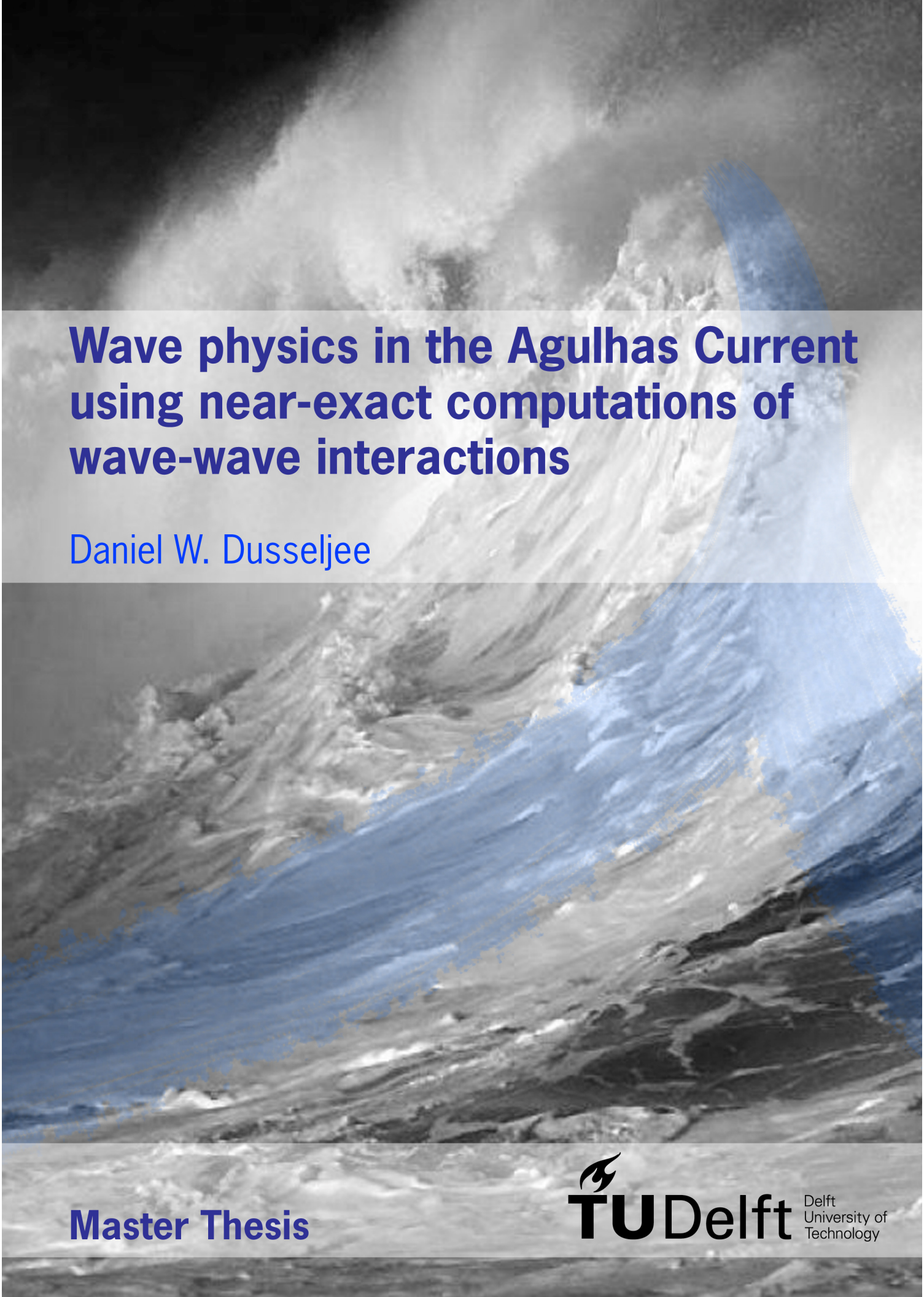

Wave physics in the Agulhas Current using near-exact computations of wave-wave interactions

Daniel W. Dusseljee

Master Thesis

TU Delft Delft University of Technology

Author

Daniël W. Dusseljee

Coenderstraat 16

2613 SM Delft

Email: Dusseljee@gmail.com

Phone: +316 41395086

Graduation committee

prof. dr. ir. G. S. Stelling

Delft University of Technology, section of Environmental Fluid Mechanics

dr. ir. L. H. Holthuijsen

Delft University of Technology, section of Environmental Fluid Mechanics

dr. ir. G. Ph. van Vledder

Delft University of Technology, section of Environmental Fluid Mechanics

dr. ir. P. H. A. J. M. van Gelder

Delft University of Technology, section of Hydraulic Engineering

ir. A. J. Lansen

Royal Haskoning, The Netherlands

Wave physics in the Agulhas Current using near-exact computations of wave-wave interactions

Daniël W. Dusseljee

May 2009

"Water has an endless horizon; there is no limitation when you look out into the water. There's nothing to interfere with the mind's eye projecting itself as far as it can possibly imagine."

Billy Joel

Preface

This thesis is the final work of my Master of Science program at the section Environmental Fluid Mechanics of the faculty Civil Engineering and Geosciences at Delft University of Technology, The Netherlands and was carried out over a period of roughly 10 months. The objective of my research was to improve insight into the wave physics in large-scale ocean currents.

I would like to thank the members of my graduation committee and the staff of the section for all the support. In particular I thank Leo Holthuijsen for the nearly daily discussions we had and Marcel Zijlema for the helpful assistance with large parallel computer systems. In addition I would like to thank Takuji Waseda, Hitoshi Tamura, Nobuhito Mori and Marten Gründlingh for their useful comments on freak waves and wave enhancement in ocean currents. Last but not least I thank my friends, my parents and Marlies who have always supported me.

Daniël W. Dusseljee
May 2009

Table of contents

1 Introduction

1.1 General background

From above, the ocean often seems a flat and blue surface. In reality however, the ocean's surface is restless and always in motion. Since Aristotle (384 - 322 B.C.), who wrote a treatise on marine biology and the relationship between wind and waves, ocean waves have been a subject of interest for many people, scientists in particular. Until now, the understanding of the mechanism of wave formation and propagation is only partly understood, because observations at sea are difficult. One of the relatively unknown phenomena at sea are freak, or rogue waves, and have gained much attention during the last decade. These extreme waves have been the subject of many sailor stories and since the extreme wave event at the Draupner platform in the North Sea in 1995 (see Figure 1.1) extensive research to this phenomenon has been carried out. This research mainly focused on the mathematical formulation of wave evolution. During the last few years, these theoretical results were compared with both numerical and laboratory observations. Freak waves are described as extremely high waves with a steep front, suddenly appearing from nowhere. They have often been related to ocean currents, as many ships encounter high waves in these areas. Wave models show that when waves encounter an opposing current, wave heights increase due to current-induced refraction of the waves. The theoretical basis of wave-current interaction has been given by Longuet-Higgins and Stewart (1961) and since then several numerical studies on the effects of currents on the propagation of waves have been carried out with the help of computer models.

The first spectral wind wave model has been produced by Gelci *et al.* (1957), introducing the concept of a spectral energy balance equation. The model described the generation and dissipation of energy in the wave spectrum and the transport of this energy in geographical space. Subsequently, the work of Miles (1957) and Phillips (1957) provided the theoretical basis for the modelling of wave generation and Hasselmann (1962) provided the basis for the nonlinear interaction between waves. The full description of this latter process (the exact computation of quadruplet wave-wave interactions) was too computationally expensive for operational wave models.

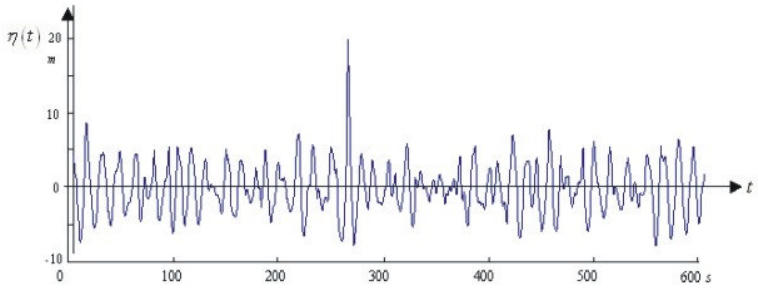

Figure 1.1: A freak wave measured at the Draupner platform in the central North Sea on 1 January 1995. The wave height of this wave was about 26 m, whereas the significant wave height was about 12 m (figure from Holthuijsen, 2007, Cambridge University Press)

Consequently, second-generation models included this process implicitly, but highly parameterized, as an additional term in the energy balance equation. Later, a numerically efficient approximation (the DIA method) of quadruplet wave-wave interactions developed by Hasselmann *et al.* (1985) led to the third-generation wave models that are used nowadays. Using this Discrete Interaction Approximation (DIA), wave models became an operational application for real life cases. The first third-generation model was WAM (WAMDI Group, 1988), in which global wave prediction in deep water (oceans and shelf seas) was possible. The first third-generation model designed to include coastal processes was SWAN (Booij *et al.*, 1999). Since Booij *et al.* (1999), significant improvements have been made in the description of the expressions for all source terms. Concerning wind input modelling; several formulations (Komen *et al.*, 1984; Yan, 1987; and Janssen, 1991) are implemented in SWAN. Concerning whitecapping dissipation, in addition to the Komen *et al.* (1984) expression, alternative formulations (Alves and Banner, 2003; Hurdle and Van Vledder, 2004; Van der Westhuysen *et al.*, 2007) are implemented as well. Concerning quadruplet wave-wave interactions, extensions to the DIA have been proposed (Van Vledder, 2001), and a near-exact method to compute these interactions was developed (Van Vledder, 2006). The latter method is the Webb-Resio-Tracy method (WRT) which is based on the original six-dimensional Boltzmann integral formulation including additions by Webb (1978), Tracy and Resio (1982) and Resio and Perrie (1991). This method is implemented in SWAN by Van Vledder, named XNL (Van Vledder and Bottema, 2003). Third-generation wave modelling is based on the energy balance equation in which all wave processes are taken into account (see manuscript and appendix A). Since Zijlema (2005) and the development of large parallel computer systems, it is now possible to compute exact quadruplet wave-wave interactions using the WRT method for a real, two-dimensional case.

The focus of this study is on the wave physics in the Agulhas Current using the third-generation numerical spectral wave model SWAN (Booij *et al.*, 1999) and the relation with the occurrence probability of freak waves in this region. To quantify the wave-current interaction processes, the intensities of all terms in the energy balance equation will be computed with SWAN as new output variables. Furthermore, we will use the WRT method for the computation of quadruplet wave-wave interactions, since the DIA is a poor approximation regarding directionality, especially for long-crested waves. It has been shown by several authors (mentioned in the manuscript) that particularly this directionality is important to determine the probability of freak waves.

We will propagate waves across two analytical cases and one more realistic numerically simulated case: (1) a straight, coastal jet, (2) an axisymmetrical ring, and (3) a fair weather case for a realistic representation of the Agulhas Current. For all three scenarios, we will use the Huygens system at SARA, Amsterdam, which is operational since August 2007. The system consists of 104 nodes with each 16 dual core processors per node, which leads to a total peak performance of 60 Teraflop/sec.

1.2 Outline

The structure of this thesis is as follows: Chapter 2 holds a (draft) manuscript that is planned to be submitted to the *Journal of Physical Oceanography*. The manuscript describes all deep water processes concerning wave-current interaction for three different scenarios, namely the above two analytical currents and one large-scale ocean current (the Agulhas Current near South Africa) and shows whether these processes influence the occurrence probability of freak waves in currents. The results for all three scenarios are presented and the manuscript concludes with a discussion and conclusions.

Additional background and details for the manuscript are provided in the appendices. Appendix A provides a general background of the deep water processes, wave-current interactions and a description of the Agulhas Current. As mentioned earlier, freak waves have often been related to the Agulhas Current. Appendix B gives an overview of the mechanisms for the generation of these waves and describes the conditions at which freak waves can occur. In SWAN, several formulations for whitecapping dissipation can be used. Appendix C gives a description of these formulations in terms of accuracy and model convergence. The theory of exact quadruplet wave-wave interactions (WRT method) and the computational times in SWAN are described in Appendix D. For the analytical ring the results using the WRT method are compared to the results for the DIA method. Finally, this thesis concludes with one-dimensional wave spectra and cross sections in the Agulhas Current that were not appropriate for publication.

2 Manuscript

Wave physics in the Agulhas Current using near-exact computations of wave-wave interactions

D. W. Dusseljee[1], L. H. Holthuijsen[2], A. J. Lansen[3], G. Ph. van Vledder[4]

[1, 2, 4] Faculty of Civil Engineering and Geosciences, Delft University of Technology, Stevinweg 1, 2628CN, Delft, The Netherlands. [1] Dusseljee@Gmail.com, [2] L.H.Holthuijsen@Tudelft.nl
[3] Royal Haskoning, Barbarossastraat 35, 6522DK, Nijmegen, The Netherlands

Abstract

Strong ocean currents such as the Agulhas Current near South-Africa are well known for the enhancement of waves and even the occurrence of freak waves. It has been suggested that the increase of wave heights in countercurrents are due to current-induced refraction. However, with the third-generation spectral wave model SWAN, which accounts for all processes of the energy balance equation, it is showed that an increase of wave heights is the result of a balance between many processes. We show these results with high-resolution computations, representing all known physical processes in two analytical cases and one more realistic numerically simulated case: (1) a straight, coastal jet, (2) an axisymmetrical ring, and (3) a fair weather case for a realistic representation of the Agulhas Current. A former suggested indicator for the occurrence of freak waves in these regions is the Benjamin-Feir Index, defined as the ratio of the wave steepness over the width of the frequency spectrum. However, numerical studies have shown that also the directionality needs to be taken into account for the probability of encountering a freak wave. Using the near-exact WRT method for the computation of quadruplet wave-wave interactions to obtain accurate directional information, it is shown in our simulations that the directional spreading is increased in countercurrents, implying a decrease of the occurrence probability of a freak wave.

2.1 Introduction

The enhancement of ocean waves in currents is well known for endangered vessels at sea (Gründlingh and Rossouw, 1995). Western-boundary currents in particular, such as the Agulhas Current in the South-West Indian Ocean and the Gulf Stream in the North Atlantic Ocean, can strongly affect ocean waves. Wave-current interactions have been described as early as the early 1960s by Longuet-Higgins and Stewart (1961) and Whitman (1962) and subsequently by Bretherton and Garrett (1969), Peregrine (1976), Gerber (1993) and Smith (2006). The interactions in the Gulf Stream and the Agulhas Current were subsequently described by Holthuijsen and Tolman (1991) and Lavrenov (1998). In these areas, the Agulhas Current in particular, there have been many reports of freak, or rogue waves (Mallory, 1974; Kharif and Pelinovsky, 2003), which led to multiple studies on wave enhancement in currents and the generation of freak waves (see for instance Smith, 1976; Gründlingh, 1994; or Gerber, 1996). Freak waves are usually described as steep and giant waves having a maximum wave height of at least two times the significant wave height (Mori and Janssen, 2004) and suddenly appearing from nowhere. One of the most important mechanisms for generating such waves is current-induced refraction (Gründlingh, 1994; Lavrenov, 1998).

The emphasis of the present study is on the wave-current interactions in the Agulhas Current using the third-generation numerical spectral wave model SWAN (Booij *et al.*, 1999) and the relation with the occurrence probability of freak waves in this region.

The basic equation of the model is the energy balance equation. Phillips (1977) shows that in deep water the energy balance equation of a fluctuating motion is:

$$\frac{\partial E}{\partial t} + \frac{\partial}{\partial x_i}\left\{E\left[U_i + \left(c_g\right)_i\right]\right\} + \Phi_{ij}\frac{\partial U_j}{\partial x_i} = 0\,, \tag{2.1}$$

where $i,j = 1,2$. $E(\sigma,\theta)$ is the energy density, distributing wave energy over (radian) frequencies σ (as observed in a reference frame moving with current velocity) and propagation directions θ (the direction normal to the wave crest of each spectral component), t is time, c_g is the group velocity and U the current velocity. As waves are strained by currents, exchange of energy occurs between the waves and the ambient flow. The last term at the left hand side in equation (2.1) represents this exchange, in which the factor Φ_{ij} is the wave-induced radiation stress. This radiation stress is equivalent to a stress acting on the water body and can be computed explicitly based upon a full expression that contains the four radiation stress components and their spatial derivatives (Phillips, 1977). To avoid computing this expression, SWAN determines the evolution of the action density $N(\sigma,\theta,x,y,t)$ instead, governed by a Eulerian formulation of the discrete spectral action balance. In spherical, geographic coordinates $\{\lambda,\varphi\}$:

$$\frac{\partial N}{\partial t} + \frac{\partial c_{g,\lambda}N}{\partial \lambda} + (\cos\varphi)^{-1}\frac{\partial c_{g,\varphi}N}{\partial \varphi} + \frac{\partial c_\theta N}{\partial \theta} + \frac{\partial c_\sigma N}{\partial \sigma} = \frac{S_{tot}}{\sigma}\,. \tag{2.2}$$

SWAN accounts for refractive propagation of waves over an arbitrary bathymetry and current field and is driven by boundary conditions, local winds and ambient currents. The first term in equation (2.2) represents the local rate of change of action density. The second and third term represent the geographic propagation, with $c_{g,\lambda}$ and $c_{g,\varphi}$ the propagation velocities in geographical space (including current-induced action bunching), the fourth term represents the propagation in spectral space, with c_θ the propagation velocity (current-induced refraction). The fifth term represents the propagation velocity in frequency space, with c_σ the propagation velocity. At the right hand side, the source term S_{tot} represents all physical processes in terms of action density. In this study we only consider deep water conditions. For deep water,

$$S_{tot} = S_{in} + S_{wcap} + S_{nl4}\,, \tag{2.3}$$

where S_{in} represents the generation by wind, S_{wcap} the dissipation by whitecapping and S_{nl4} the nonlinear quadruplet wave-wave interactions. All of these processes are formulated in a reference frame moving with the current (thus implying the use of the relative wind speed).

In default mode, SWAN uses the wind input and whitecapping expressions of Komen *et al.* (1984), in which the wind input is based on Snyder *et al.* (1981) and whitecapping dissipation is based on Hasselmann (1974). However, Van der Westhuysen *et al.* (2007) show that the accuracy of SWAN can be improved by using a whitecapping dissipation based on Alves and Banner (2003), in combination with a wind input term based on Yan (1987). Moreover, in our study we found that using the formulation of Komen *et al.* (1984) in strong countercurrents, the model did not converge, whereas the model properly converged using the formulation of Van der Westhuysen *et al.* (2007). We therefore adopted the latter formulation in our computations.

Besides current-induced refraction, another mechanism that has been suggested for generating freak waves is nonlinear focusing (Alber, 1978; Dysthe, 1979). In a wave group, with only a few waves, one wave can develop into a single, exceptionally large freak wave. Several studies (see for instance Onorato *et al.*, 2001; Janssen, 2003; and Onorato *et al.*, 2005) have suggested that the probability occurrence of a freak wave increases as the spectral shape becomes narrower. In the conventional approach of wave statistics, this is ignored and the probability is given by the Raleigh distribution. However, Janssen (2003) describes this self-focusing in terms of the Benjamin-Feir Index (BFI), which accounts for the steepness of the waves and their degree of randomness. However, recent studies (Waseda, 2006; Waseda *et al.*, 2008; Mori *et al.*, 2009) show that in addition to the BFI, also the directionality of the waves needs to be taken into account to quantify the increased probability of encountering a freak wave. They show that only a small increase in directional spreading significantly reduces the probability of encountering a freak wave. For instance, according to Mori *et al.* (2009), a directional distribution (with a directional spreading of $\sigma_\theta = 30°$) reduces the effect on the freak wave occurrence probability by a factor 30, compared to unidirectional waves. To obtain accurate directional information and to reproduce a precise spectral shape, we will use the near-exact method of Tracy and Resio (1982) based on Webb (1978) for the computations of the quadruplet wave-wave interactions, generally known as the WRT method [1]. The expression for these interactions, in terms of a Boltzmann integral, was formulated by Hasselmann (1962). This theory considers resonant

[1] In terms of computational capacity, an accurate numerical computation of these interactions is prohibitively expensive. Hasselmann *et al.* (1985) therefore developed the Discrete Interaction Approximation (DIA) method, which reproduces the slow downshifting of the peak frequency and the shape stabilization during wave growth. However, the DIA is not able to properly represent the nonlinear transfer rate in comparison with a (near-)exact solution of the Boltzmann integral (Van Vledder and Bottema, 2003). The DIA is a poor approximation regarding directionality, especially for long-crested waves (Holthuijsen *et al.*, 2008). Furthermore, Van der Westhuysen *et al.* (2007) found a better estimate of the Pierson and Moskowitz (1964) equilibrium level in wave growth and more accurate details of the directional distribution using the WRT method.

interactions between sets of four wavenumbers $\vec{k}_1, \vec{k}_2, \vec{k}_3$ and $\vec{k}_4$. Van Vledder (2006) coded this method in a subroutine from the host wave prediction model in SWAN. The WRT method has proven to produce significantly narrower directional distributions than other methods (Van der Westhuysen *et al.*, 2007). Also, the distributions become bi-model at higher frequencies, as observed in the field by Hwang *et al.* (2000). Furthermore, in our study we found that the computed directional distributions contained small wiggles at the energy containing tail ($\sigma/\sigma_p > 2$). These wiggles imply propagating waves against the mean wave direction, which we consider impossible. The effect of the wiggles on the directional spreading will be presented.

We propagate waves across two analytical cases and one more realistic numerically simulated case: (1) a straight, coastal jet, (2) an axisymmetrical ring, and (3) a fair weather case for a realistic representation of the Agulhas Current. We show several characteristic wave parameters to quantify the effects of the currents on the waves as well as geographic distributions of the intensities of all terms in the energy balance equation.

2.2 Current, wave and wind conditions

The South Equatorial Current in the Indian Ocean is deflected southward by the continental shelf of Africa and the Coriolis Effect. It eventually develops into the Agulhas Current. In the northern part of the Agulhas Current (between 27°S and 34°S), the current flows with a high speed jet down the continental coast. Once the current has moved past Port Elizabeth and starts following the mild continental slope of the Agulhas Bank, current velocities decrease and large meanders and cyclonic eddies develop. Past the southern tip of the African continental shelf, the Agulhas Current turns back on itself in a tight loop, called the Agulhas Current Retroflection. Here, strong anticyclonic eddies develop due to cold Sub-Antarctic wedges. These rings may slowly move westward, losing their distinct surface thermal expression (Lutjeharms and Van Ballegooyen, 1988).

The **first analytical current field** represents the coastal jet. Lavrenov (1998) gives an analytical description based upon observations of Schumann (1976). These observations show large velocity gradients at the shore side and smaller gradients at the ocean side. As we only want to use this current field to inspect some generic wave characteristics, we slightly adapted the analytical description and replaced the asymmetric gradients with equal, medium velocity gradients on both sides to obtain a symmetrical current (Figure 2.1). The current increases in positive y-direction from 0 m s^{-1} to 2.2 m s^{-1} at 800 km distance, after which it remains constant, and decreases in both x-directions. The expressions are given in Appendix A.

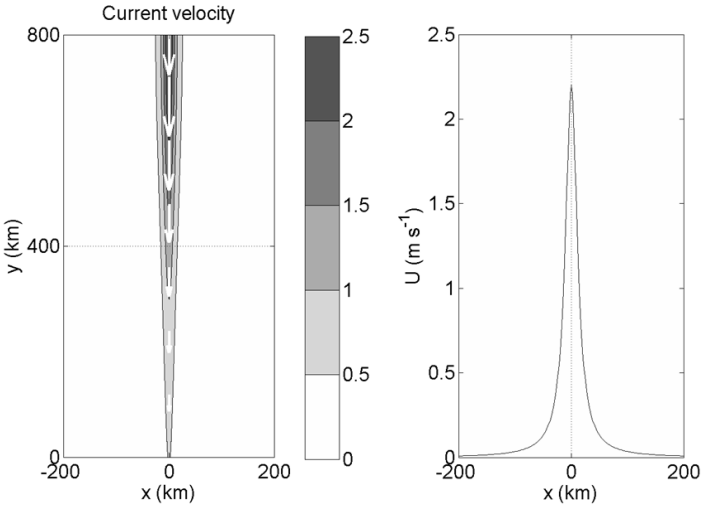

Figure 2.1: Current field with velocities (in m s^{-1}) of the analytical jet current (left panel) and velocity profile for y = 800 km with a maximum velocity of 2.2 m s^{-1} based on the analytic description of Lavrenov (1998) (right panel).

The **second analytical current field** represents an anticyclonic ring. The velocity field that we used is based on an ocean ring obtained from the real-time nowcast/forecast of the NRL Layered Ocean Model (NLOM) with a geographic resolution of 1/32° (Figure 2.2). The NLOM uses atmospheric forcing from the Navy Operational Global Atmospheric Prediction System (NOGAPS) and assimilation of SST and satellite altimeter data obtained via the NAVOCEANO Altimeter Data Fusion Center and operates only in waters deeper than 200 m.

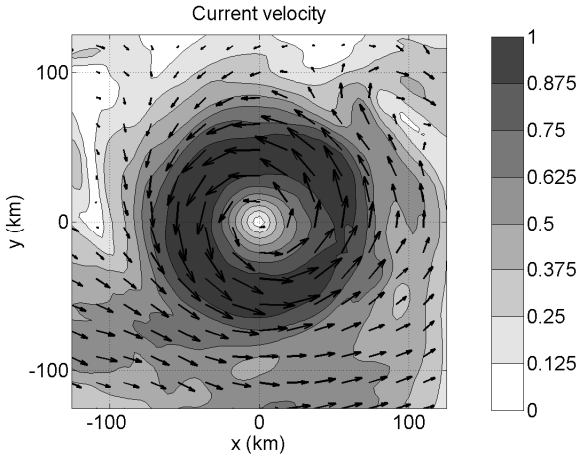

Figure 2.2: Current field with velocities (in m s^{-1}) of an anticyclonic (anti clockwise in the Southern Hemisphere) ocean ring on Oct. 2nd, 2001, in the vicinity of the Agulhas retroflection near 12°E; 41°S with a diameter of 200 km and a maximum velocity of about 1.0 m s^{-1}.

To find this ring, we inspected a set of three months of daily averaged hindcast data. The current field of 2 October 2001 was selected because it showed highest current velocities and velocity gradients. For the same reasons as above, we approximated this ring with an analytical expression, given in Appendix A. The corresponding current field is given in Figure 2.3. The radius to maximum velocity (1.0 m s^{-1}) is 50 km with a parabolic velocity profile centered on this maximum.

For both analytical cases, we used a wind speed $U_{10} = 15$ m s^{-1} blowing in the positive y-direction. Waves enter the current at the up-wind boundary with a JONSWAP spectrum with a $\cos^2(\theta)$ directional distribution and a significant wave height of $H_s = 3$ m and a peak period of $T_p = 7$ sec, propagating in the same direction as the wind. To reduce any boundary effects, the computational boundaries were located far from the area with non-zero currents. The computational grid was 1200 × 1200 km^2 and the mesh size was 2 × 2 km^2.

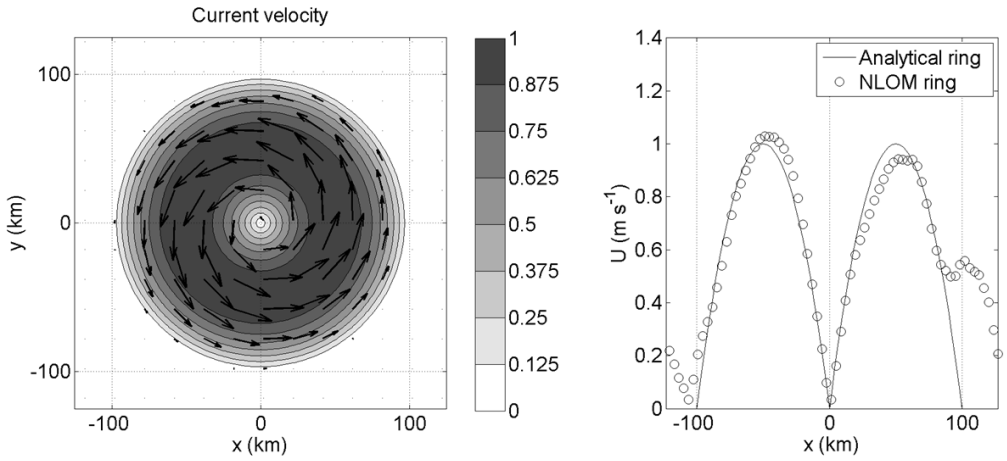

Figure 2.3: Current field with velocities (in m s^{-1}) of the analytical ring current based on the NLOM ocean ring (left panel) and a cross section through $y = 0$ with a maximum velocity of 1.0 m s^{-1} (right panel), compared to the NLOM ocean ring of Figure 2.2.

For the **third, realistic current field of the entire Agulhas Current system**, we used the area from 10°E to 35°E and from 25°S to 45°S on Oct. 2nd, 2001 of the NLOM model for the Agulhas Current (Figure 2.4). The wind and wave boundary conditions for our computations have been chosen independently from the true conditions on this day. They have been chosen in such a way that the waves oppose the currents in regions where the current velocities are highest and such that the ratio of the phase velocity over current velocity in these regions is in the order of 1/5. As a result of this, wave blocking may be expected. We used a uniform wind speed of $U_{10} = 15$ m s^{-1} and a wind direction of 45° (Cartesian convention). Waves enter the current with the same JONSWAP spectrum as above, propagating in the wind direction.

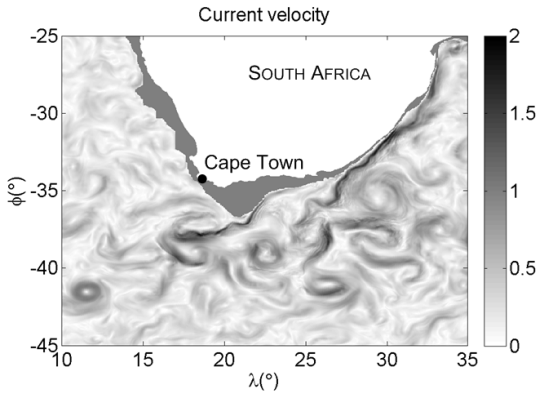

Figure 2.4: Current field with velocities (in m s^{-1}) of the Agulhas Current on Oct. 2nd, 2001 from the NLOM ocean model with maximum velocities of about 2.0 m s^{-1} in the coastal jet (between 30° S and 35° S) and 1.0 m s^{-1} in the anticyclonic ring near 12°E; 41°S.

2.3 Results

2.3.1. Computed quantities

To quantify the effects of the currents on the waves, we consider the significant wave height H_s (m), the mean wavelength L_m (m), the mean wave direction θ (°, in Cartesian convention), and the directional width of the spectrum (°). In addition to characteristic wave parameters, we also show the geographic distributions of the intensity of all terms in the energy balance (i.e. including the energy transfer between waves and currents): (1) wind generation, (2) whitecapping, (3) nonlinear quadruplet wave-wave interactions, (4) propagation in x,y-direction, (5) propagation in θ-direction, (6) propagation in σ-direction and (7) work done by the current against the radiation stress. The latter is given separately in the last section. We define these intensities as the integral over the spectral domain of the absolute value of the term under consideration. The basic reason to take the absolute value here is to include the quadruplet wave-wave interactions. These interactions are conservative for both energy and action, and the integral itself would be zero.

2.3.2. Results for the coastal jet

In the jet, the significant wave height H_s (Figure 2.5) increases from the upwave boundary in positive y-direction (downwind) from 3.0 m to 5.5 m. When we compare this to a reference point outside the current field, perpendicular to the central axis of the jet, the significant wave height is 4.7 m, due to an increasing fetch. Initially, the average wave direction in the jet is the y-direction (90°). However, the jet refracts the waves from outside the current field towards its axis by about 5°, which is clearly visible in Figure 2.5. As the opposing current velocity increases, the directional spreading increases correspondingly from about 30° to 40°, but we have reason to question this since the wiggles in the directional distribution (i.e. waves propagating against the average wave direction) are still included (see next section). In the jet, one would expect the wavelength L_m to decrease, due to the fact that the waves slow down. However, as follows from Figure 2.5, it slightly increases, especially over the gradients of the current from 60 m to 65 m. The effect of the waves slowing down on the wavelength is thus relatively small compared to the opposite effect of the addition of low-frequency energy to the spectrum due to the quadruplet wave-wave interactions. As a result of the relatively large increasing wave height and the less increasing wavelength, the steepness in the jet increases by a factor of 1.08 to a maximum of 0.088.

The geographic distributions for the coastal jet are given in Figure 2.6. All three deep-water source terms show a considerable increase in intensity as the waves propagate through the jet. From the upwave boundary, the generation by wind at the centre of the jet increases from 3.0×10^{-4} m^2 s^{-1} to 5.1×10^{-4} m^2 s^{-1} in downwind direction due to the increase of the relative wind speed (i.e. the absolute wind speed plus the current velocity). Outside the jet, the generation by wind only slightly increases to 3.3×10^{-4} m^2 s^{-1}. As a result of the increase in steepness, whitecapping dissipation increases in the jet from 3.1×10^{-4} m^2 s^{-1} to 6.0×10^{-4} m^2 s^{-1}, instead of a maximum whitecapping dissipation of 3.6×10^{-4} m^2 s^{-1} outside the jet. The increase in steepness in the jet also results in more nonlinear waves, and thus an increase in nonlinear quadruplet interactions. Outside the jet, the intensity of these interactions remains constant at 2.0×10^{-4} m^2 s^{-1}. In the jet, the intensity increases to a maximum of 3.5×10^{-4} m^2 s^{-1}. The latter distribution shows the intensity of the redistribution of energy in the spectrum from the mid-range frequencies to lower frequencies and a small fraction to higher frequencies, thus shifting the peak of the spectrum to lower frequencies. The intensities of the propagation in geographical x,y-space (energy bunching), in frequency σ-space (frequency-shift) in directional θ-space (refraction) increase as well, in particular in the gradients of the current. However, the intensities for these terms are about half the intensity of the source terms. As becomes clear from the distributions for the significant wave height, the wave direction and the wavelength, waves propagating in the axis of the jet, do not refract and thus their wave rays are straight lines. This results in relatively smaller intensities of the propagation terms in the axis of the jet (Figure 2.6).

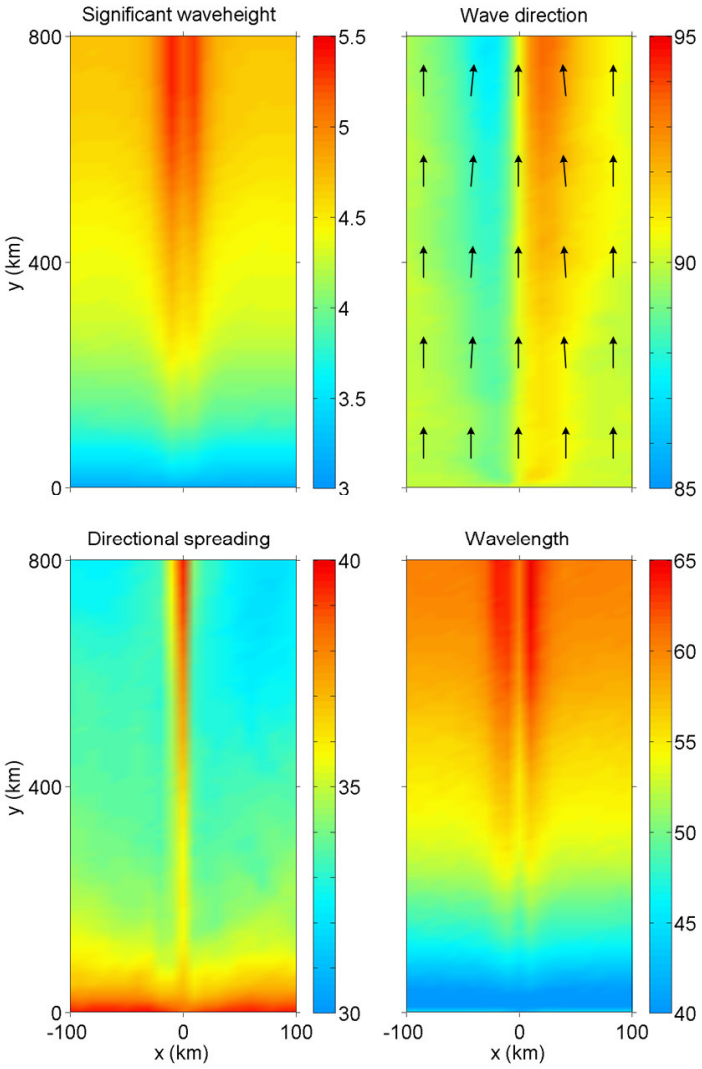

Figure 2.5: Geographic distributions of the significant wave height (m) and the wave direction (°, Cartesian) (top row), and the directional spreading (°) and wavelength (m) (bottom row) for the analytical coastal jet using the WRT method.

From the upwave boundary, the propagation in geographical space increases from 0.6×10^{-4} $m^2\,s^{-1}$ outside the jet to 2.5×10^{-4} $m^2\,s^{-1}$ in the gradient of the jet. This is due to the decrease of the propagation velocity of the waves in the jet and is equivalent to the effect of shoaling in shallow waters. Due to the opposing current, the propagation in frequency space increases from zero outside the jet to a maximum of 1.4×10^{-4} $m^2\,s^{-1}$ in the jet, accounting for the current-induced Doppler frequency shift. Finally, the propagation in directional space increases from zero to a maximum of 2.5×10^{-4} $m^2\,s^{-1}$ in the jet and accounts for the current-induced refraction.

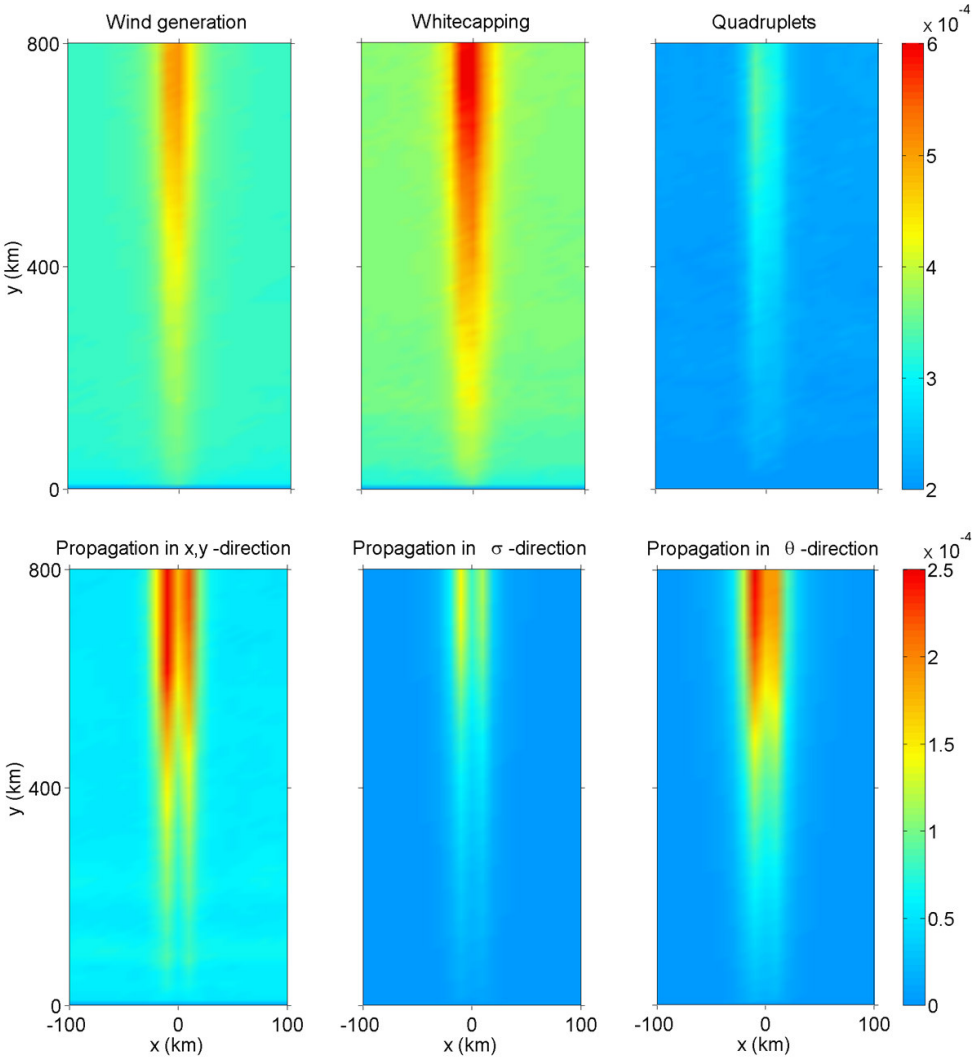

Figure 2.6: Geographic distributions of the intensity of the source terms (top row) and the propagation terms (bottom row) for the analytical coastal jet using the WRT method.

2.3.3. Results for the analytical ring

In the ring, the significant wave height H_s (Figure 2.7) increases at the left-hand side (i.e. seen in the direction of wave propagation, with an opposing current) from 4.5 m to 5.1 m and decreases at the right-hand side (i.e. with a following current) to 3.9 m, as would be expected from linear wave theory. As for the coastal jet, the average wave direction outside the ring is the y-direction (90°). At the left-hand side, the current refracts the waves towards the central axis of the opposing current by about 5°, similar to that of the jet. At the right-hand side the opposite effect occurs. Due to the following current, the wave rays diverge by about 5°. Somewhat down-wave of the ring, the directional spreading increases at the left-hand side from 34° to 38° and decreases at the rind-hand side to about 31°. As mentioned earlier, the directional distributions using the WRT method contain small wiggles at the energy containing tail ($\sigma/\sigma_p > 2$). These wiggles imply propagating waves against the mean wave direction, which we consider impossible. When these wiggles are removed from the directional distributions, the overall directional spreading decreases with approximately 5° compared to the values above (see Appendix B). The wavelength increases at the left-hand side from 58 m to 64 m and decreases at the right-hand side to 52 m. The steepness in the ring increases at the left-hand side by a factor of 1.08 to 0.084 and decreases at the right-hand side by a factor of 1.05 to 0.074.

The geographic distributions for the analytical ring are given in Figure 2.8. At the left-hand side, the source terms increase in intensity, as the current is opposite to the waves. The results are similar to those of the coastal jet, although the intensities are somewhat smaller, due to smaller velocities (maximum velocity of 1.0 m s^{-1} instead of 2.2 m s^{-1}). At the right-hand side, all source terms decrease in intensity. The generation by wind increases from 3.3 $\times$ 10^{-4} m^2 s^{-1} to 4.3 $\times$ 10^{-4} m^2 s^{-1} due to the increase of the relative wind speed. As the following current at the right-hand side decreases the relative wind speed, the generation of wind decreases as well to 2.3 $\times$ 10^{-4} $m^2 s^{-1}$. Similar, whitecapping increases from 3.6 $\times$ 10^{-4} m^2 s^{-1} to 5.0 $\times$ 10^{-4} $m^2 s^{-1}$ at the left-hand side and decreases at the right-hand side to 2.5 $\times$ 10^{-4} m^2 s^{-1}. The nonlinear quadruplet interactions increase at the left hand-side from 2.0 $\times$ 10^{-4} $m^2 s^{-1}$ to 3.0 $\times$ 10^{-4} $m^2 s^{-1}$ and decrease at the right-hand side to 1.5 $\times$ 10^{-4} $m^2 s^{-1}$. As for the coastal jet, the propagation terms increase in intensity in the lateral gradients of the current. The ring refracts the incoming waves and energy bunches in the opposing side of the current, as becomes clear from the distribution of the propagation in geographical space. From the upwave boundary, the intensity increases from 0.6 $\times$ 10^{-4} $m^2 s^{-1}$ outside the ring to 1.0 $\times$ 10^{-4} $m^2 s^{-1}$ in the gradient of the opposing current. The propagation in frequency space (Doppler frequency shift) increases from zero outside the ring to a maximum of 0.4 $\times$ 10^{-4} m^2 s^{-1} in the opposing current. Finally, the propagation in directional space (refraction) increases from zero to a maximum of 0.7 $\times$ 10^{-4} $m^2 s^{-1}$ in the gradients of the ring.

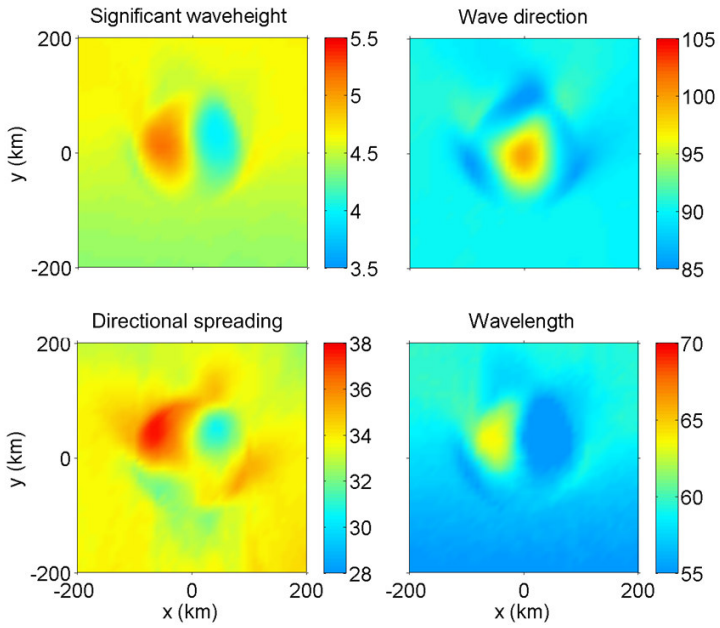

Figure 2.7: Geographic distributions of the significant wave height (m) and the wave direction (°, Cartesian) (top row), and the directional spreading (°) and wavelength (m) (bottom row) for the analytical ring using the WRT method.

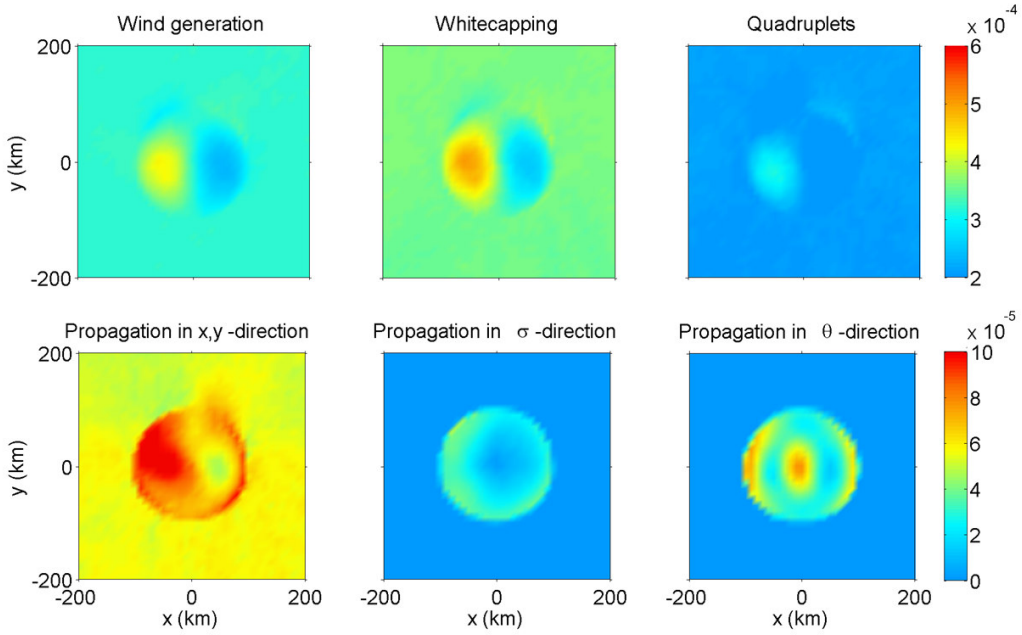

Figure 2.8: Geographic distributions of the intensity of the source terms (top row) and the propagation terms (bottom row) for the analytical ring using the WRT method.

2.3.4. Results for the Agulhas Current

The results for the computation of the Agulhas Current with the velocity field of NLOM are essentially as expected. They are given in Figure 2.9 and Figure 2.10. In areas of large current velocity gradients, the significant wave height H_s increases up to a factor of 1.3, especially in areas of an opposing current. This is similar to the results of the two previous cases. The local change in wave direction and directional spreading in areas of large current velocity gradients as seen in the previous cases is reproduced in the situation with the NLOM data velocity field, although the continental shelf influences these parameters significantly near the coast. The geographic pattern of the wavelength closely follows the pattern of the currents, with increasing wavelengths by a factor 1.15 in opposing currents and decreasing wavelengths by a factor 0.85 in following currents. As a result, the steepness increases by a factor 1.08 in opposing currents and decreases by a factor 0.95 in following currents.

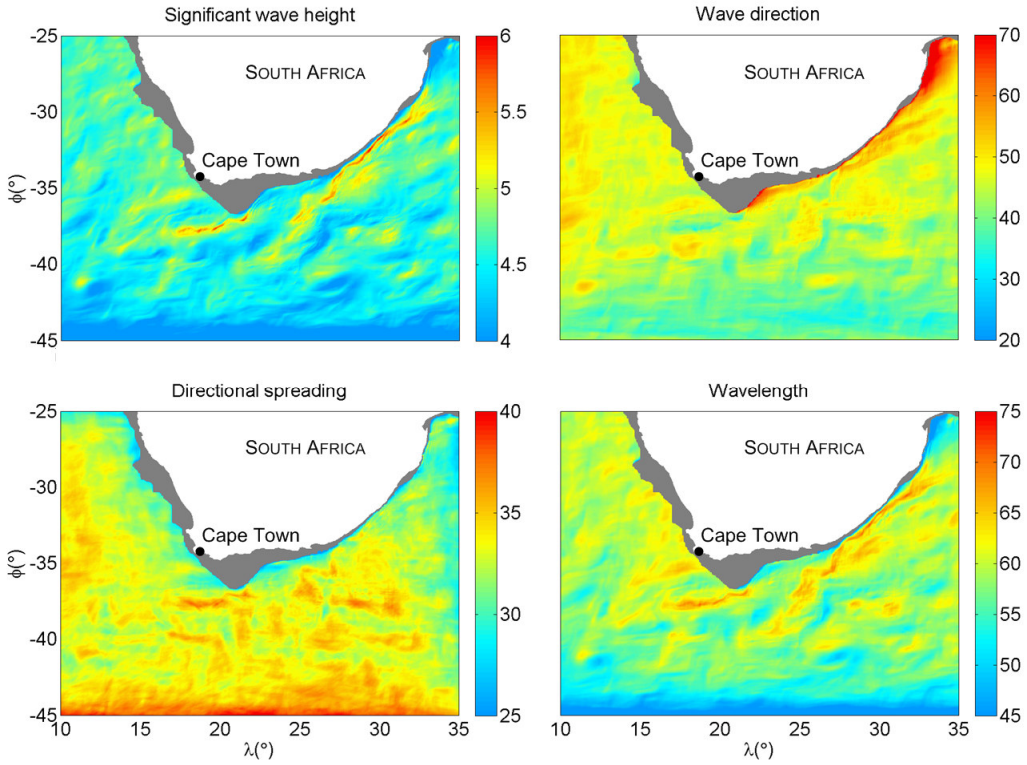

Figure 2.9: Geographic distributions of the significant wave height (m) and the wave direction (°, Cartesian) (top row), and the directional spreading (°) and the wavelength (bottom row) in and near the Agulhas Current for a uniform wind (U_{10} = 15 m s^{-1} from 45°, Cartesian) and a uniform wave boundary condition (significant wave height of H_s = 3.0 m and a peak period of T_p = 7.0 sec, propagating in the same direction as the wind) using the WRT method.

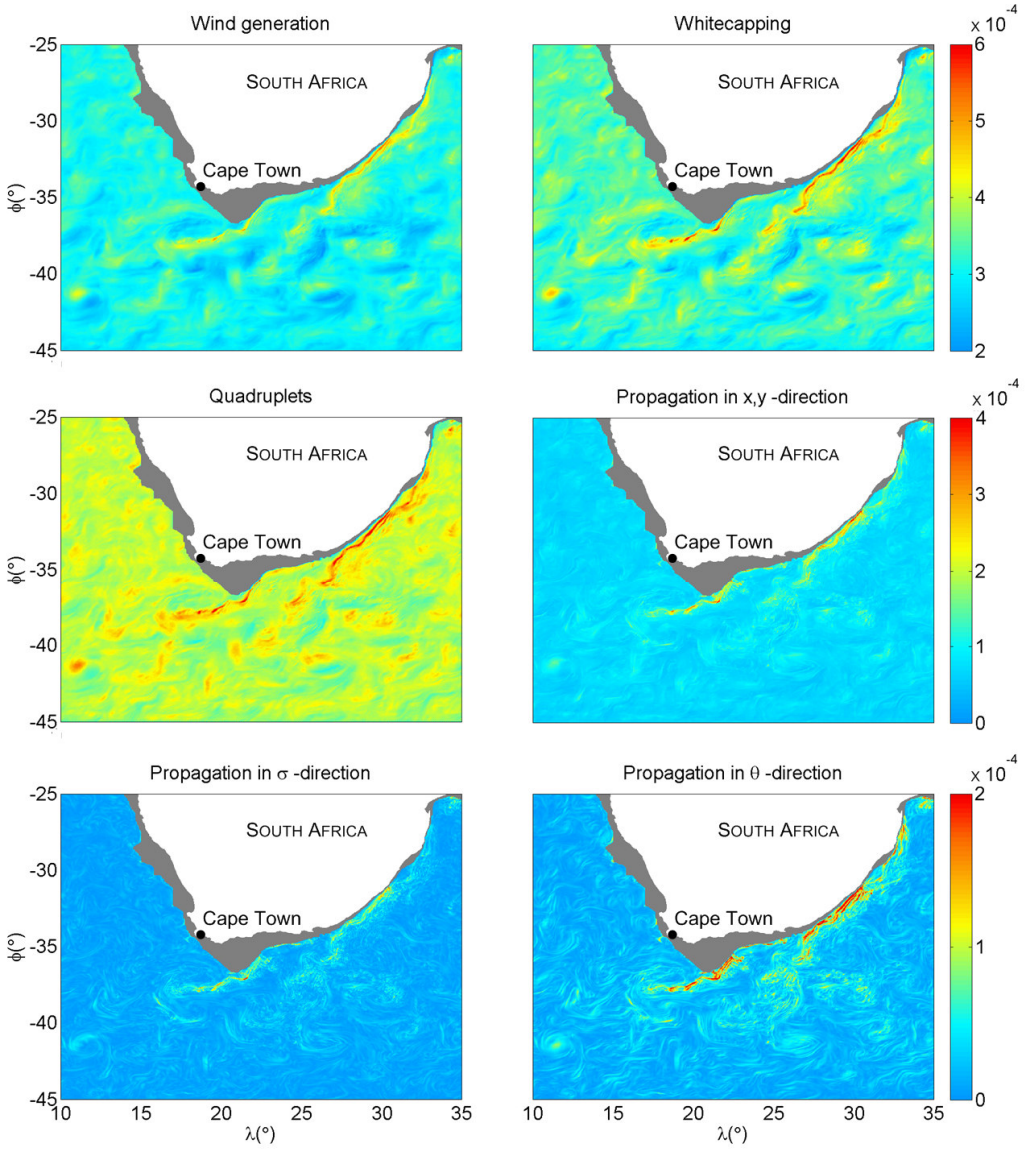

Figure 2.10: Geographic distributions of the intensity of the source terms and propagation terms in and near the Agulhas Current for a uniform wind (U_{10} = 15 m s^{-1} from 45°, Cartesian) and a uniform wave boundary condition (significant wave height of H_s = 3.0 m and a peak period of T_p = 7.0 sec, propagating in the same direction as the wind) using the WRT method.

The intensities of the source terms, representing the generation by wind, whitecapping dissipation and quadruplet wave-wave interactions, show similar patterns. These processes are relatively more active in regions where the waves oppose the currents than in regions where they follow the currents. In the coastal jet (between 30° S and 35° S), the generation by wind increases by a factor 1.75, whitecapping dissipation by a factor of 2.1 and the quadruplet wave-wave interactions by a factor 2.0. The increase of these processes is also

found in the anticyclonic ring near 12°E; 41°S, although slightly smaller due to smaller velocities (maximum velocity of 1.1 m s^{-1}). These results confirm the findings of the two previous, analytical cases. The geographic distributions of the intensity of the propagation in geographical x,y-space, accounting for the energy bunching, and the propagation in frequency space, accounting for the Doppler frequency shift, closely follow the pattern of the currents as well. The pattern of the current-induced refraction is similar to these patterns, with the same concentration on the gradients of the currents. Outside the currents, the two latter terms are zero, as refraction and frequency shifting are not present.

2.3.5. Work done against the radiation stress

For the Agulhas Current, the work done of the current against the radiation stress is presented by the integral over the spectral domain of the absolute value of the rest term, see Figure 2.11:

$$S_{ij}\frac{\partial U_j}{\partial x_i} = \iint \left| S_{tot} - \frac{\partial E}{\partial t} - \nabla_{\vec{x}}\left[E\left(\vec{c}_g + \vec{U}\right)\right] - \nabla_{(\sigma,\theta)}\left[E\left(\vec{c}_{(\sigma,\theta)}\right)\right] \right| \mathrm{d}\sigma\mathrm{d}\theta \tag{2.4}$$

The intensity of this term is again relatively more active in regions where the waves oppose the currents than in regions where they follow the currents. The work done of the current against the radiation stress increases to a maximum of 1.5 × 10^{-5} m^2 s^{-1} in the gradients of the coastal jet. Also, the magnitude of this term is one order smaller than the magnitudes of the other processes.

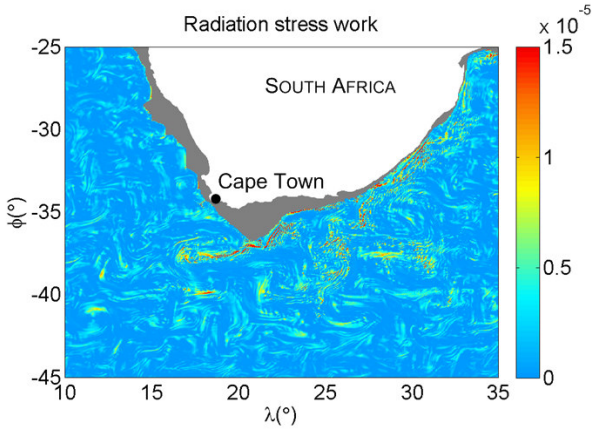

Figure 2.11: Geographic distribution of the intensity the work done of the current against the radiation stress in and near the Agulhas Current for a uniform wind (U_{10} = 15 m s^{-1} from 45°, Cartesian) and a uniform wave boundary condition (significant wave height of H_s = 3.0 m and a peak period of T_p = 7.0 sec, propagating in the same direction as the wind) using the WRT method.

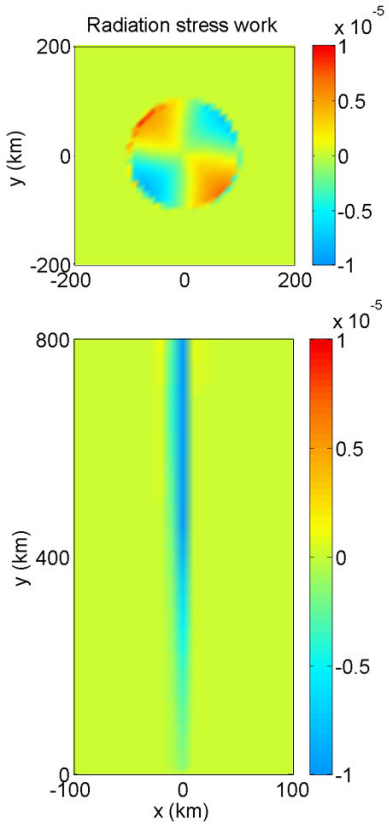

Figure 2.12: Geographic distributions of the intensity of the work done of the current against the radiation stress for the analytical ring (top) and the coastal jet (bottom) using the WRT method.

For the two analytical cases, we considered this term not as the absolute value of the rest term, but as the real value instead, see Figure 2.12. The sign gives us information whether the current acts against the radiation stress of the waves or the contrary. As for the propagation terms, the work done of the current against the radiation stress is largest in the gradients of the current and zero outside the current. In the jet, the negative sign indicates that energy is transferred from the waves to the current, leading to decreasing wave heights. In the analytical ring, the nicely axisymmetrical pattern shows that this is true in the top right and the bottom left quadrants. In the top left and the bottom right quadrants, the opposite occurs; energy is transferred from the current to the waves, leading to increasing wave heights.

2.4 Discussion and conclusions

We used the third-generation numerical spectral wave model SWAN to compute characteristic wave parameters and the geographic distributions of the intensity of all terms in the energy balance for two analytical current cases and one realistic representation of the Agulhas Current in the South-West Indian Ocean. We used the near-exact WRT method for the computation of the nonlinear quadruplet wave-wave interactions in combination with the saturation-based model by Van der Westhuysen *et al.* (2007) for the computation of whitecapping dissipation. In the coastal jet (Figure 2.1), it was found that the intensity of the source- and propagation terms increased. As a result, more energy was added to the spectrum, and thus the wave heights in the jet increased. The following processes contribute to the increase in wave energy:

1) Current-induced refraction causes a change in wave direction towards the central axis of the jet. The wave paths converged in the jet, thus concentrating incoming and locally generated wave energy.
2) Due to the increase in relative wind speed and slightly steeper waves in the jet, the generation by wind increased, adding more energy to the spectrum.

In the jet, one would expect a decrease in wavelength due to a decrease in phase velocity (Longuet-Higgins and Stewart, 1961). However, it was shown that the wavelength of the waves in the jet increased. This is due to the fact that wave blocking at the higher frequencies and the addition of low-frequency energy to the spectrum due to quadruplet wave-wave interactions had more effect than the current-induced up-shifting of the wave-frequencies. Although this increase in wavelength, the steepness increased as well due to the relative larger effect of the increasing wave heights due to energy bunching and refraction. The above processes were counteracted by (1) the increased whitecapping dissipation in the jet as a result of the steeper waves, and (2) the transfer of energy from the waves to the current due to the work against the radiation stress, but these were less profound than the former processes. We showed that all processes are in the same order of magnitude, except for the work done of the current against the radiation stress, which is one order of magnitude smaller.

The results for the analytical ring (Figure 2.3) showed that in areas with opposing currents, all processes were qualitatively similar to those of the coastal jet. In areas with following currents on the other hand, the opposite effects occurred. This corresponds with the findings of Holthuijsen and Tolman (1991). In the ring, a nicely axisymmetrical pattern develops for the work done against the radiation stress due to the four radiation stress components and

their spatial derivatives (Phillips, 1977). Since we wanted to know the intensity of this term, we computed the latter term as the rest term when all other terms were computed. However, to completely understand the axisymmetrical pattern, the four components and their spatial derivatives need to be computed explicitly.

For the Agulhas Current, we showed that the wave-current interaction processes are similar to those of the two analytical cases. The results in the coastal jet (between 30° S and 35° S) and the anticyclonic ring (near 12°E; 41°S) confirm the general picture that waves get trapped in a countercurrent and that wave heights are increased. Our work shows that the variation in intensity of the occurring processes in the entire region is closely related to the pattern of the current velocity, suggesting that the increase in wave height is not only due to current-induced refraction (as previously assumed), but is the result of a balance between all processes. We expect this is true in all major ocean currents.

Outside the current, directional spreading is decreased over an increasing fetch due to frequency-dispersion (e.g. see Figure 2.9). However, all three cases showed that in a countercurrent, the directional spreading is increased by a factor of about 1.2. As mentioned in the introduction (and the references therein), this increase would imply a decrease of the occurrence probability of a freak wave (see Mori *et al.*, 2009), and thus this would suggest that the effect of nonlinear focusing in currents, as a mechanism to describe the generation of freak waves, is smaller in countercurrents, thus contradicting earlier results (see authors mentioned in introduction).

Acknowledgements

We would like to thank the U.S. Naval Research Laboratory for granting us permission to use their numerically simulated velocity fields of the Agulhas Region, which were carried out with exceptionally high geographic resolution. Furthermore, we thank Marcel Zijlema, Takuji Waseda and Hitoshi Tamura for interesting comments and assistance. This work was sponsored by the Stichting Nationale Computerfaciliteiten (National Computing Facilities Foundation, NCF) for the use of supercomputer facilities, with financial support from the Nederlandse Organisatie voor Wetenschappelijk Onderzoek (Netherlands Organization for Scientific Research, NWO).

Appendix A

Analytical jet

Velocity component ($y < 800$ km)	*Velocity component ($y \geq 800$ km)*
$U_x = 0$	$U_x = 0$
$U_y = b/\left(\left(1 + ay^2\right)\left(1 + c(x-\mu)^2\right)\right)$	$U_y = b/\left(1 + c(x-\mu)^2\right)$

In which $a = 0.6 \times 10^{-11}$ m^{-2}, $b = 2.2$ m s^{-1}, $c = 6.26 \times 10^{-9}$ m^{-2} and $\mu = 2.0 \times 10^{5}$ m.

Analytical ring

Velocity component ($y < 0$)	*Velocity component ($y \geq 0$)*
$U_x = +y\left(a\left(x^2 + y^2\right)^{0.5} + b\right)$	$U_x = -y\left(a\left(x^2 + y^2\right)^{0.5} + b\right)$
$U_y = -x\left(a\left(x^2 + y^2\right)^{0.5} + b\right)$	$U_y = -x\left(a\left(x^2 + y^2\right)^{0.5} + b\right)$

In which $a = -4/R^2$ m^{-2}, $b = 4/R$ m^{-1} and $R = 2.0 \times 10^{5}$ m.

Appendix B

To visualize the effects of the WRT method for the computation of the quadruplet wave-wave interactions compared to the DIA, we also used the latter method in the analytical ring. Figure b. gives the one-dimensional spectrum at three locations in the current. Both the DIA and the WRT show a peak downshift when waves enter the countercurrent. However, using the DIA, the spectrum shows smaller energy densities, thus implying smaller significant wave heights. Also the peak frequency for the DIA is lower than for the WRT. These results correspond with the results found by Van der Westhuysen (2007).

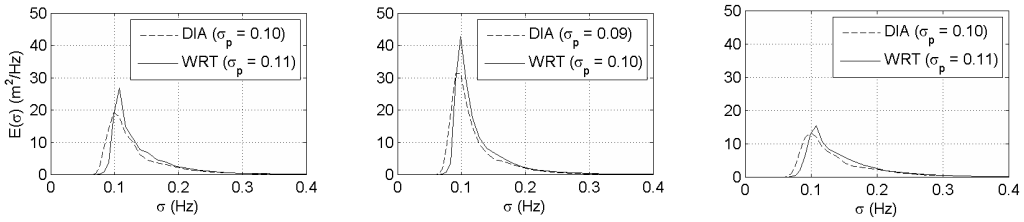

Figure b.1: One-dimensional wave spectra with the according peak frequencies for the analytical ring using the DIA and the WRT method outside the current (left), in the centre of the opposing current (middle) and in the centre of the following current (right).

In comparison to the DIA, the WRT method gives significantly narrower directional distributions, especially for the energy-containing tail (Figure b.). Furthermore, the WRT method is able to generate a bi-modal distribution (as observed by Hwang *et al.*, 2000), as is also shown by Van der Westhuysen *et al.* (2005). The small wiggles in the directional distributions at the energy containing tail ($\sigma/\sigma_p \geqslant 2$) were removed, as we considered these physically impossible. The adjusted directional distributions showed a decrease in directional spreading of about 5°, as is shown in Table b.1.

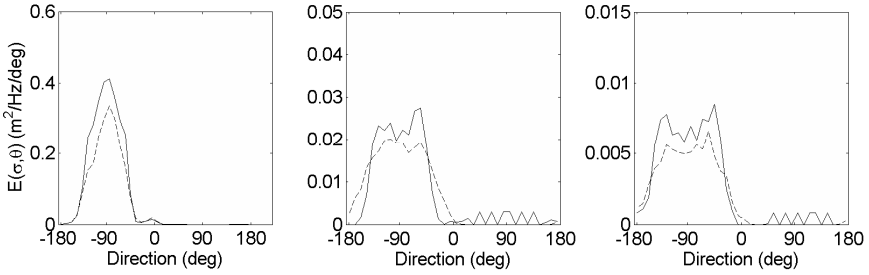

Figure b.2: Directional distributions at the peak (left, $\sigma/\sigma_p = 1$) and energy-containing tail (middle, $\sigma/\sigma_p = 2$; and right $\sigma/\sigma_p = 2.6$) produced using the DIA (dashed line) and the WRT method (solid line) outside the current.

Table b.1: Directional spreading at three locations in the analytical ring for the different methods.

	σ_θ (°) *DIA*	σ_θ (°) *WRT*	*Adjusted* σ_θ (°)*WRT*
No current	31.94	31.68	26.87
Opposite current	35.38	33.51	30.64
Following current	30.66	30.95	25.99

References

Alber, I. E., 1978, The effect of randomness on the stability of two-dimensional surface wave trains, *Proc. Roy. Soc. A*, **363**, 528

Alves, J. H. G. M. and M. L. Banner, 2003, Performance of a saturation-based dissipation-rate source term in modelling the fetch-limited evolution of wind waves, *J. Phys. Oceanography*, **33**, 6, 1274-1298

Booij, N., R. C. Ris and L. H. Holthuijsen, 1999, A third-generation wave model for coastal regions, Part I, Model description and validation, *J.Geoph. Res.*, **104**, C4, 7649-7666

Bretherton, F. P., and C. J. R. Garrett, 1969, Wavetrains in inhomogeneous moving media, *Proc. Roy. Soc.* A., **302**, 1471, 529-554

Dysthe, K. B., 1979, Note on a modification to the nonlinear Schrodinger equation for application to deep water waves, *Proceedings of the Royal Society of London. Series A, Mathematical and Physical Sciences*, **369**, 1736, 105-114

Gerber, M., 1993, The interaction of deep-water gravity waves and an annular current: linear theory, *Journal of Fluid Mechanics*, **248**, 153-172

Gerber, M., 1996, Giant waves and the Agulhas Current, Deep-Sea Res. (submitted)

Gründlingh, M. L., 1994, Evidence of surface wave enhancement in the southwest Indian Ocean from satellite altimetry, J. Geophys. Res., **99**, C4, 7917–7927

Gründlingh, M. L., and M. Rossouw, 1995, Wave attenuation in the Agulhas Current, *South African J. of Science*, **91**, 7, 357-361

Hasselmann, K., 1962, On the non-linear transfer in a gravity wave spectrum, part 1: General theory, *J. Fluid Mech.*, **12**, 481-500

Hasselmann, K., 1974, On the spectral dissipation of ocean waves due to white capping, *Boundary-Layer Meteorol.*, **6**, 1-2, 107-127

Hasselmann, S., K. Hasselmann, J. H. Allender and T. P. Barnett, 1985, Computations and parameterizations of the non-linear energy transfer in a gravity wave spectrum, part 2: Parameterizations of the non-linear transfer for application in wave models, *J. Phys. Oceanography*, **15**, 11, 1378-1391

Holthuijsen, L. H., and H. L. Tolman, 1991, Effects of the Gulf Stream on ocean waves, *J. Geophys. Res.,* **96**, C7, 12755–12771

Holthuijsen, L. H., N. Booij, R. C. Ris, I. Haagsma, A. T. M. M. Kieftenburg, E. E. Kriezi, M. Zijlema, and A. J. van der Westhuysen, 2008, SWAN – User Manual, Technical report, Delft University of Technology, Environmental Fluid Mechanics Section, available from http://vlm089.citg.tudelft.nl/swan/index.htm (Version 40.72)

Hwang, P. A., D. W. Wang, E. J. Walsh, W. B. Krabill, and R. N. Shift, 2000, Airborne measurements of the wavenumber spectra of ocean waves. Part 2. Directional distribution, *J. Phys. Oceanography*, **30**, 2768-2787

Janssen, P. A. E. M., 2003, Non-linear four-wave interactions and freak waves, *J. Phys. Oceanography*, **33**, 4, 863-884

Kharif, C., and E. Pelinovsky, 2003, Physical mechanisms of the rogue wave phenomenon, *European Journal of Mechanics B/Fluids*, **22**, 603–634

Komen, G. J., S. Hasselmann and K. Hasselmann, 1984, On the existence of a fully developed wind-sea spectrum, *J. Phys. Oceanography*, **14**, 1271-1285

Lavrenov, I. V., 1998, The wave energy concentration at the Agulhas Current off South Africa, *Natural Hazards*, **17**, 2, 117-127

Longuet-Higgins, M. S., and R. W. Stewart, 1960, Changes in the form of short gravity waves on long waves and tidal currents, *Journal of Fluid Mechanics*, **8**, 4, 565-583

Longuet-Higgins, M. S., and R. W. Stewart, 1961, The changes in amplitude of short gravity waves on non-uniform currents, *Journal of Fluid Mechanics*, **10**, 4, 529-549

Lutjeharms, J. R. E., and R. C. van Ballegooyen, 1988, The retroflection of the Agulhas Current, *J. Phys. Oceanography*, **18**, 11, 1570–1583

Mallory, J. K., 1974, Abnormal waves on the south east coast of South Africa, *Int. Hydrog. Rev.*, **51**, 99-129

Mori, N., and P. A. E. M. Janssen, 2004, Dependence of freak wave occurrence on kurtosis. Rogue Waves 2004, Brest, France. Not published

Mori, N., M. Onorato, and P. A. E. M. Janssen, 2009, Directional dispersion effects on kurtosis for freak wave prediction, Rogue Waves 2008, Brest, France. Not published

Onorato, M., A. R. Osborne, and M. Serio, 2001, Extreme wave events in directional, random oceanic sea states, *Phys. Fluids*, **14**, 4, 25-28

Onorato, M., A. R. Osborne, and M. Serio, 2005, On deviations from Guassian statistics for surface gravity waves, *Proceedings Rogue Waves, Hawaiian Winter Workshop*, 79-83

Peregrine, D.H., 1976, Interaction of water waves and currents, *Adv. Appl. Math.*, **16**, 9-117

Pierson, W. J., Jr., and L. Moskowitz, 1964, A proposed spectral form for fully developed wind seas based on the similarity theory of S. A. Kitaigorodskii, *J. Geophys. Res.*, **69**, 24, 5181–5190

Phillips, O. M., 1977, The dynamics of the upper ocean, Cambridge University Press, 336 pp.

Schumann, E. H., 1976, High waves in the Agulhas Current, *Mariners Weather Log.*, **20**, 1, 1-5

Smith, R., 1976, Giant waves, *J. Fluid Mech.*, **77**, 3, 417-431

Smith, J. A., 2006, Wave-current interactions in finite depth, *J. Phys. Oceanography*, **36**, 7, 1403-1419

Snyder, R.L., Dobson, F.W., Elliott, J.A., and R.B. Long, 1981, Array measurement of atmospheric pressure fluctuations above surface gravity waves, *J. Fluid Mech.*, **102**, 1-59

Tracy, B. A., and D. T. Resio, 1982, Theory and calculation of the nonlinear energy transfer between sea waves in deep water, Technical report, WIS Report 11, US Army Corps of Engineers

Vledder, G. Ph. van, and M. Bottema, 2003, Improved modelling of nonlinear four-wave interactions in shallow water, *Proc. 28th Int. Conf. Coastal Engineering*, ASCE, 459–471

Vledder, G. Ph. van, 2006, The WRT method for the computation of non-linear four-wave interactions in discrete spectral wave models, *Coastal Engineering*, **53**, 223–242

Waseda, T., 2006, Impact of directionality on the extreme wave occurrence in a discrete random wave system, *Proc. 9th Int. Workshop Wave Hindcasting and Forecasting*, Victoria, Canada

Waseda, T., T. Kinoshita and H. Tamura, 2008, Evolution of a random directional wave and freak wave occurrence, *J. Phys. Oceanography,* Preliminary issue

Webb, D. J., 1978, Non-linear transfers between sea waves, *Deep-Sea research*, **25**, 3, 279-298

Westhuysen, A. van der, M. Zijlema, and J.A. Battjes, 2005, Improvement of the numerics and deep-water physics in an academic version of SWAN, *Proc. 29th Int. Conf. Coastal Engineering, ASCE*, 855-867

Westhuysen, A. van der, M. Zijlema and J.A. Battjes, 2007, Nonlinear saturation-based white capping dissipation in SWAN for deep and shallow water, *Coastal Engineering*, **54**, 2, 151-170

Whitman, G. B., 1962, Mass, momentum and energy flux in water waves, *Journal of Fluid Mechanics*, **12**, 1, 135-147

Yan, L., 1987, An improved wind input source term for third-generation ocean wave modelling, Scientific Report WR-No 87-8, De Bilt, KNMI

Appendix A

Background

This appendix gives general background information regarding the deep water wave processes and the interaction of waves and currents. In the first section (A.1), the wave spectrum and the energy balance equation, which are the key concepts for describing and modelling waves, are briefly discussed and all terms in this equation are described.[2] Basic equations that govern wave-current interaction are described in the second section (A.2) and the third section (A.3) of this appendix gives a brief description of the origin of large-scale ocean currents in the Indian Ocean, the Agulhas Current in particular.

A.1 Processes at deep water

For a description of the energy balance equation, first the variance density spectrum (interpreted as the energy density spectrum) needs to be introduced. To fully describe ocean waves, the chaotic sea surface is treated as the summation of a large number of (harmonic) wave components, each with a constant amplitude and a phase randomly chosen for each realization of a wave record. This spectral method, the random-phase/amplitude model, is the basis for the wave spectrum. Wave records, measured either with in situ instruments (buoys, wave poles or ships), or remote sensing instruments (high above the ocean, e.g., laser or radar airplanes and satellites), consider the surface elevation $\eta(t)$ at one location as a function of time. According to the random phase/amplitude model, these wave records can be reproduced as the summation of N harmonic wave components, with

$$\eta(t) = \sum_{i=1}^{N} a_i \cos(\sigma_i t + \alpha_i)\,. \tag{A.1}$$

[2] It is noted that the wave spectrum and the energy balance equation are trivial concepts in this field of research. Section A.1 is a quick review for those not acquainted with these terms. The description and the derivation of the wave spectrum and the energy balance equation are thoroughly explained in many textbooks concerning (ocean) waves (e.g. Holthuijsen, 2007).

Herein, a_i and α_i are the amplitude and random phase, respectively, and σ_i the radian frequency of the i^{th} wave component for a given wave record. For each of these frequencies, the values for the amplitude and phase can be determined. This leads to the amplitude (and phase) spectrum. The phase spectrum can be ignored since the phases turn out to always have any value between 0 and 2π without any preference for any value. The amplitude spectrum therefore remains to characterize the wave record. The amplitude spectrum, however, fails in describing physical properties such as wave energy and also, the sum of the amplitudes is not equal to the amplitude of the sum. It is therefore more meaningful to distribute the variance $\frac{1}{2}a_i^2$ of each wave component. The variance spectrum is still discrete, whereas all frequencies are present at sea. In order to obtain a continuous distribution for all frequencies, the variance is distributed over the frequency interval $\Delta\sigma$, giving a variance density $\frac{1}{2}a_i^2/\Delta\sigma$. By letting the frequency interval $\Delta\sigma$ approaching zero, the definition of the variance density spectrum becomes

$$E_{variance}(\sigma) = \lim_{\Delta\sigma\to 0} \tfrac{1}{\Delta\sigma} E\left\{\tfrac{1}{2}a_i^2\right\}. \tag{A.2}$$

The variance density spectrum gives a complete description of the surface elevation of ocean waves in a statistical sense. Wave propagation implies that water particles move, thus representing kinetic energy. When they move up or down, this requires work against gravitation, and thus representing potential energy. The total time-averaged wave-induced energy is $E = \frac{1}{2}\rho g a^2$, from which it follows that the energy density spectrum can be obtained with $E_{energy}(\sigma) = \rho g E_{variance}(\sigma)$. The one-dimensional variance density spectrum characterizes the stationary (Gaussian) surface elevation as a function of time. To describe the actual, three-dimensional, moving waves, the horizontal *x,y* dimension needs to be added. This addition leads to the two-dimensional frequency-direction spectrum $E(\sigma,\theta)$. A normalized cross-section trough this spectrum at a given frequency gives the directional distribution, with $D(\theta) = E(\sigma,\theta)/E(\sigma)$. Ocean wave models compute this two-dimensional spectrum for a large number of locations in the ocean simultaneously with the local energy balance at each of these locations (or grid cells). The change of energy in a cell is the net import of wave energy due to wave propagation combined with the generation of wave energy and thus for each cell, for each wave component and at each moment in time, the energy balance equation is given by

$$\begin{aligned}&\frac{\partial E(\sigma,\theta;x,y,t)}{\partial t} + \frac{\partial\, c_{g,x}E(\sigma,\theta;x,y,t)}{\partial x} + \frac{\partial\, c_{g,y}E(\sigma,\theta;x,y,t)}{\partial y} + \\ &+ \frac{\partial\, c_\theta E(\sigma,\theta;x,y,t)}{\partial \theta} + \frac{\partial\, c_\sigma E(\sigma,\theta;x,y,t)}{\partial \sigma} + \Phi_{ij}\frac{\partial U_j}{\partial x_i} = S_{tot}(\sigma,\theta;x,y,t)\end{aligned} \tag{A.3}$$

The first term represents the local rate of change. The second and third term represent the geographic propagation in which the energy propagation velocities are given by $c_{g;x} = c_g \cos\theta + U_x$ and $c_{g;y} = c_g \sin\theta + U_y$, in which $c_g = \partial\sigma / \partial k$ is the group velocity and (U_x, U_y) represents the current velocity. In case of shallow water, or in our case the presence of a current, the balance includes other terms. When waves enter a current, an individual wave component changes direction and thus propagates through a three-dimensional x,y,θ-space. The directional turning of the waves (refraction) is added to the energy balance as the fourth term accounting for energy moving from one direction to another in the directional distribution $D(\theta)$. The current-induced rate of turning c_θ is given by $c_\theta = -\partial U_n / \partial m$, where U_n is the current component normal to the wave crest, and m a coordinate along the wave crest.

Besides the effect of refraction (and energy bunching accounted by the wave propagation terms in geographical space), the Doppler-like frequency-shifting is included in the energy balance as a propagation term in frequency space (fifth term). The propagation velocity in frequency space is given by $c_\sigma = -c_g k \cdot \partial U_n / \partial n$ (Holthuijsen, 2007), in which k is the wave number and n is a coordinate normal to the wave crest. As waves are strained by currents, exchange of energy occurs between the waves and the ambient flow. The last term at the left hand side in equation (A.3) represents this exchange, in which the factor Φ_{ij} is the wave-induced radiation stress tensor and U_j is the current vector. This radiation stress is equivalent to a stress acting on the water body and can be computed explicitly based upon a full expression that contains the four radiation stress components ($i,j \in \{\lambda,\varphi\}$) and their spatial derivatives (Phillips, 1977):

$$\Phi_{ij} \frac{\partial U_j}{\partial x_i} = \Phi_{\lambda\lambda} \frac{\partial U_\lambda}{\partial \lambda} + \Phi_{\lambda\varphi} \frac{\partial U_\varphi}{\partial \lambda} + \Phi_{\varphi\lambda} \frac{\partial U_\lambda}{\partial \varphi} + \Phi_{\varphi\varphi} \frac{\partial U_\varphi}{\partial \varphi} \tag{A.4}$$

Finally, the locally generated energy is represented by the source term S_{tot} representing all effects of generation by wind, whitecapping dissipation and quadruplet wave-wave interactions.

As follows from equation (A.3), energy density is not conserved in presence of ocean currents due to the work of the current against the radiation stress. At the moment, wave models (such as the SWAN model) do not compute the radiation stress components explicitly but, instead, use the action density $N(\sigma,\theta,x,y,t)$ balance equation instead of the energy density balance equation. The action density is defined as $N = E / \sigma$ and along a path in four-dimensional phase space (x,y,σ,θ), the action density N is conserved.

In terms of spherical, geographic coordinates $\{\lambda,\varphi\}$, the action balance can be written as (Komen *et al.*, 1984):

$$\frac{\partial N}{\partial t} + \frac{\partial c_{g,\lambda} N}{\partial \lambda} + (\cos\varphi)^{-1} \frac{\partial c_{g,\varphi} N}{\partial \varphi} + \frac{\partial c_\theta N}{\partial \theta} + \frac{\partial c_\sigma N}{\partial \sigma} = \frac{S_{tot}}{\sigma}, \tag{A.5}$$

in which λ and φ are longitude and latitude, respectively. The group velocity components in longitude and latitude directions are respectively $c_{g,\lambda} = c_g \sin\theta / (R\cos\varphi)$ and $c_{g,\varphi} = c_g \cos\theta / R$, and the rate of turning of the wave direction is given by $c_\theta = c_g \sin\theta \tan\varphi / R$, where R is the earth's radius. When all terms in (A.5) are computed, the work done by the current against the radiation stress can be computed as the rest term of locally generated energy (source terms) and the energy balance terms, so

$$\Phi_{ij} \frac{\partial U_j}{\partial x_i} = \iint \left(S_{tot} - \frac{\partial E}{\partial t} + \nabla_{\vec{x}} \left[E(\vec{c}_g) + \vec{U} \right] + \nabla_{(\sigma,\theta)} \left[E(\vec{c}_{(\sigma,\theta)}) \right] \right) \mathrm{d}\sigma \mathrm{d}\theta \,. \tag{A.6}$$

This can also be derived from the action balance (Phillips, 1977). The energy balance equation (A.3) can be derived from the conservation principle with, for deep water $c^2 = g/k$, $\sigma^2 = gk$ and $c_g = \frac{1}{2}c$. Combining (A.5) and $N = E/\sigma$, the interaction term becomes

$$N \frac{\partial \sigma}{\partial t} = \frac{\partial E}{\partial t} - S_{tot} \,. \tag{A.7}$$

With, for deep water,

$$\frac{\partial \sigma}{\partial t} = c_\sigma = -\tfrac{1}{2} ck \frac{\partial U_j}{\partial x_i} \,, \tag{A.8}$$

this results in

$$N \frac{\partial \sigma}{\partial t} = \frac{E}{\sigma} k_i (c_g)_j \frac{\partial U_j}{\partial x_i} = \tfrac{1}{2} E \left(l_i l_j \right) \frac{\partial U_j}{\partial x_i} \,, \tag{A.9}$$

in which $l_{ij} = k_{ij}/k$ is a unit vector in the direction of the wave propagation. From the first-order wave solutions, Phillips (1977) shows that (A.9) is consistent with the expression for the radiation stress $\Phi_{ij} = \frac{1}{2} E \left(l_i l_j \right)$, resulting in

$$N \frac{\partial \sigma}{\partial t} = \tfrac{1}{2} E \left(l_i l_j \right) \frac{\partial U_j}{\partial x_i} = \Phi_{ij} \frac{\partial U_j}{\partial x_i} = \frac{\partial E}{\partial t} - S_{tot} \,, \tag{A.10}$$

And thus the work done of the current against the radiation stress can be computed as the rest term, when all terms are computed, see equation (A.6).

A.2 Wave-current interaction

Wave-current interactions have been described as early as the early 1960s by Longuet-Higgins and Stewart (1961). They showed that the kinematics of a train of surface gravity waves in the presence of a current is characterized by a wavenumber k and the relative frequency component σ. The dispersion relation gives the functional dependence of σ on k and for linear deep-water waves:

$$\sigma^2 = gk\,. \tag{A.11}$$

For a fixed reference frame, the absolute frequency ω_0 is

$$\omega_0 = kU + \sigma = const., \tag{A.12}$$

in which U is the current velocity. With the dispersion relation for deep water and $c^2 = g/k$ this leads to $k(U + c) = k_0 c_0$, where k_0 and c_0 denote the wavenumber and wave velocity in a fixed reference frame. From this equation, Longuet-Higgins and Stewart (1961) derived the equation for the phase velocity c, resulting in

$$\frac{c}{c_0} = \frac{1}{2}\left[1 + \sqrt{1 + \frac{4U}{c_0}}\right], \tag{A.13}$$

and due to $k/k_0 = (c/c_0)^{-2}$ this implies a change in wavelength. When the current velocity becomes equal and opposite to the local group-velocity for deep water $c_g = \frac{1}{2}c$, waves can no longer propagate against the current, and will break before this point is reached (wave blocking). With $c_g = g/4\pi\sigma$ this leads to the relation between the current velocity and the relative frequency, see Figure A.1.

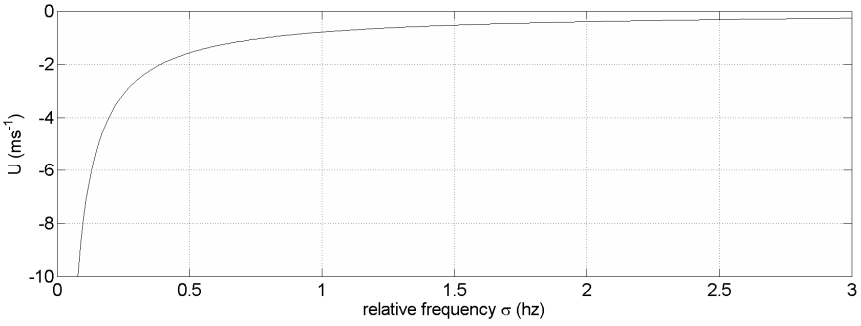

Figure A.1: Wave blocking frequency against current velocity for a countercurrent.

From the energy balance, Longuet-Higgins and Stewart (1961) also derived that in absence of wave breaking, the local amplitude a is given by:

$$\frac{a}{a_0} = \frac{c_0}{\sqrt{c\,(c + 2U)}}\,. \tag{A.14}$$

While the phase velocity c is decreasing, the energy flux of the wave motion is increasing and therefore the wave height is increasing (energy bunching; equivalent to shoaling in shallow water). Furthermore, equation (A.13) implies that for waves travelling against a current, the propagation velocity and wavelength decrease. From (A.12), it follows that for waves travelling *against* the current, their relative frequency increases, and because $k = \sigma^2/g$, the current-induced frequency shift can be written as

$$\sigma = \omega - \frac{\sigma^2}{g} U\,. \tag{A.15}$$

This Doppler shift results in a displacement of spectral components and, as follows from (A.15), especially occurs in the higher frequencies. In opposing currents the spectral maximum displaces to lower frequencies, whereas the high frequency tail of the spectrum becomes steeper, due to wave blocking (Lavrenov, 2003).

Energy bunching and frequency shifting can thus well be described using the linear theory. However, when deep water waves cross an area with a variable current, refraction takes place, which complicates the situation. If there are no abrupt discontinuities in current velocity, the application of geometrical optics theory (Kenyon, 1971) has shown that wave rays are curved and the direction and magnitudes of the wave numbers continuously change along the wave ray. Due to this effect, waves get trapped or strained in the current, see Figure A.2.

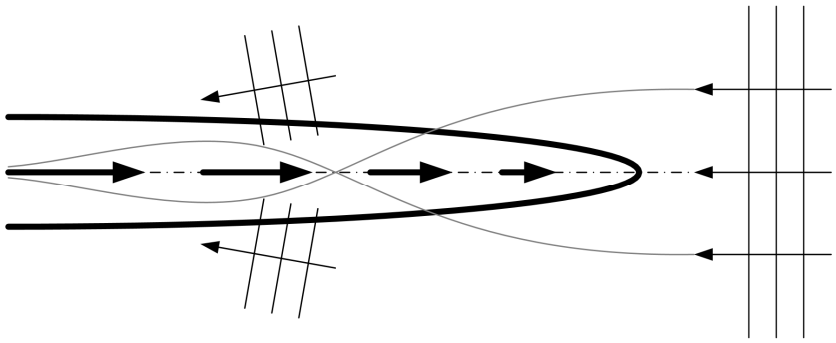

Figure A.2: Current-induced refraction of waves.

A countercurrent acts as an optical lens where energy may be focused at certain crossing points. Wave rays can cross each other, forming a complicated pattern of crossing points. The envelopes of neighboring rays are generally known as caustics. White and Fornberg (1998) calculated such a pattern for a ring, see Figure A.3.

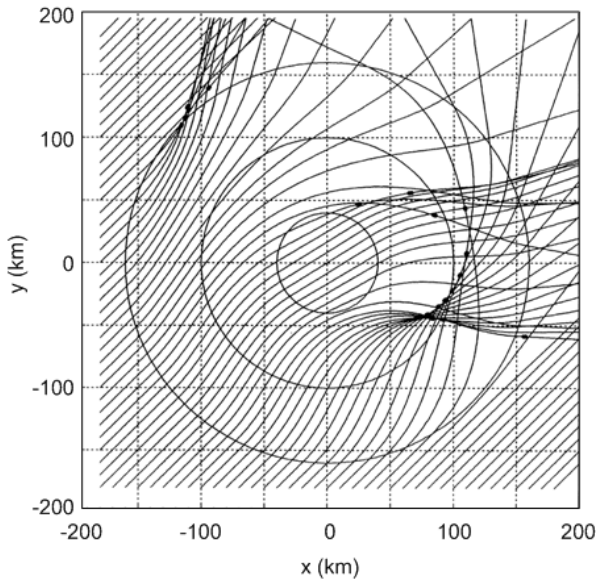

Figure A.3: Rays of waves moving into a current. The rays are calculated by White and Fornberg (1998) using the current profile from Gerber (1993).

By using wave-ray techniques in the Agulhas Current, Lavrenov (1998) found that waves moving upstream can get trapped in the jet as it becomes narrower north of East London, see Figure A.4. The red and black rays correspond to waves with an initial 20° difference in propagation directions. In our study, the effect of wave-crossings and caustics is not considered, but SWAN does consider the refraction of the energy for each frequency component. Furthermore, for realistic ocean environments, the effects of caustics are diffused by the random character and short-crestedness of ocean waves; see for instance Holthuijsen and Tolman (1991).

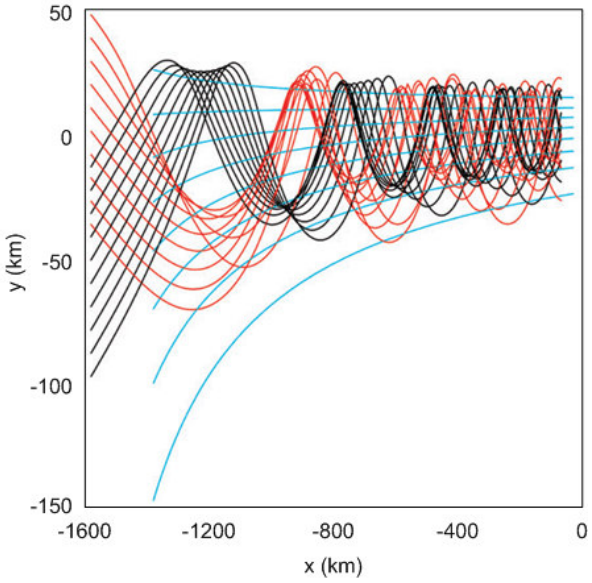

Figure A.4: Rays of waves moving upstream into a widening current jet. The current field (blue streamlines) is similar to that of Lavrenov (1998) for the Agulhas Current. Figure by Dysthe *et al.* (2008).

A.3 Description of the Agulhas Current

During the southern summer (from November to March), the equatorial surface circulation in the Indian Ocean is similar to that in the other oceans. Due to extensive solar heating at the equator, air rises and is being transported towards the subtropics, where the air descends to the surface. From here, the air flows back to the equator. This circulation pattern is called the Hadley Cell. Due to the Coriolis Effect, the equatorward winds turn to the right in the Northern Hemisphere and to the left in the Southern Hemisphere and therefore blow to the west. These trade winds set in motion the water masses between the tropics and thus two Equatorial Currents are developed; a North Equatorial Current (NEC) and a South Equatorial Current (SEC).[3] Such currents travel along the equator worldwide. Deflection by the Coriolis Effect and deflection along the continental shelf of Africa direct these currents usually away from the equator. However, during southern summer, the SEC is deflected to the south and the NEC piles up at the eastern shelf of Africa from where it slowly flows back as the Equatorial Counter Current (ECC), shown in Figure A.5. This is due to the fact that the Coriolis Effect is relatively small. The SEC develops as a warm western boundary current into the Agulhas Current.

[3] In fact, the actual process that sets water masses in motion is the wind-induced breaking of waves in deep water, better known as whitecapping. The breaking of waves results in a net flow of water in the same direction as the wind.

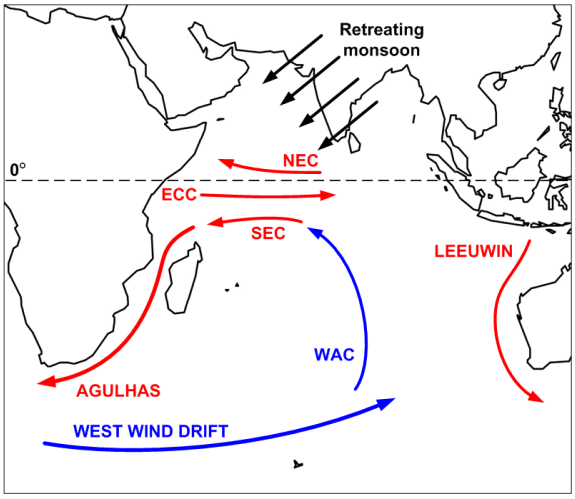

Figure A.5: Indian Ocean circulation during southern summer (November – March). The westward South Equatorial Current (SEC), the North Equatorial Current (NEC) and the Equatorial Counter Current (ECC) are similar to the equatorial currents in the other oceans.

Between 30° and 60° latitude, surface winds blow from the high pressure areas (around 60°) towards the poles. These winds, called Westerlies, are predominantly from the southwest in the Southern Hemisphere and from the northwest in the Northern Hemisphere, again due to the Coriolis Effect. The Westerlies can be particularly strong in the Southern Hemisphere, where there is less land in these latitudes. The strongest of these winds come from the Roaring Forties, between 40 and 50 degrees latitude. The Westerlies set in motion the water masses in the cold Antarctic (the West Wind Drift) and completes the gyre. The West Australian Current (WAC) turns northward out of the West Wind Drift and eventually merges with the SEC.

During southern winter (from May – September), the surface circulation in the Indian Ocean is different due to the southwestern monsoons, see Figure A.6. Due to extensive heating, air pressure is low at the northern and central Indian subcontinent. Winds, full of moisture, blow from the Indian Ocean over the subcontinent into the void. In the north, the Himalayas act as a wall, which forces these winds up. The air gets cooler and precipitation occurs (monsoon rains). During this season, the NEC disappears and is replaced by the Southwest Monsoon Current (SMC), which flows in eastern direction along the Indian subcontinent. Due to the south-western monsoon winds, the Somali Current (SC) can develop, which feeds the SMC. Along the Australian coast, the Leeuwin Current flows south from the warm areas of South-East Asia, and is therefore responsible for the mild climate in south-western Australia. Due to the Leeuwin Current, the WAC is displaced further offshore.

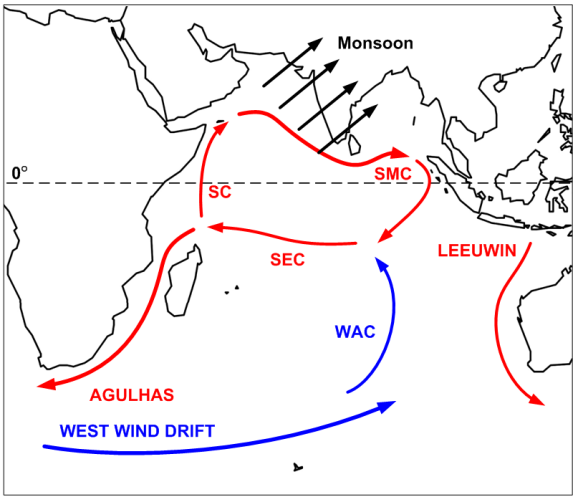

Figure A.6: Indian Ocean circulation during southern winter (May – September). The South Equatorial Current (SEC) deflects along the African shelf into the Somalia Current and the Southwest Monsoon Current (SMC).

In the Mozambique Channel between Mozambique and Madagascar, the southward flow is very complex, due to a persistent field of mesoscale gyres that lies west of Madagascar (Seatre and Jorge da Silva, 1984). Just passed Madagascar, at the border of South-Africa and Mozambique, the Agulhas Current can be considered steady and continuous. During southern winter, a southward flow occurs at the east coast of Madagascar, feeding into the Agulhas Current as well. However, the Agulhas Current shows very little seasonal variability, since the Madagascar Current also flows from the SEC.

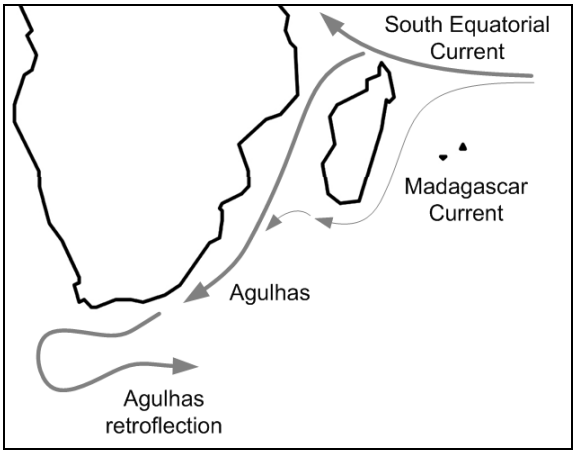

Figure A.7: Surface currents for the South-West Indian Ocean during southern winter.

Between 27° and 34° S the Agulhas Current remains constant along the continental shelf of Africa, reaching velocities up to 2.5 ms^{-1}. At more southern latitudes, the Agulhas Current becomes weaker but also diverges in a fan-shaped manner (Atlas of the Atlantic and Indian Ocean, 1977). Also, current velocities decrease and large meanders develop. Further south, just west of Cape Town, the current does not flow straight into the Atlantic Ocean. Instead, it makes a U-turn back into the Indian Ocean, in the direction of Australia, called the Agulhas retroflection. As the current retroflects, rings of about 100 to 300 km are incidentally pinched off. These anticyclonic rings move westward and are the main contributor to upper ocean transport of water between the Indian and Atlantic Ocean. By way of the Benguela Current, these rings are transported to the northwest and thus ocean temperatures in the south Atlantic and even weather patterns in these regions are greatly affected. About six rings are developed per year (Lutjeharms and Van Ballegooyen, 1988). During June until August, strong low pressure systems often develop near Antarctica and travel rapidly to the northeast. These south-western winds from the Roaring Forties can produce large waves that can be dangerous to vessels at sea.

The velocity field of the Agulhas Current that we used in our computations was obtained from the real-time nowcast/forecast of the NRL Layered Ocean Model (NLOM) with an exceptionally high resolution of 1/32°. NLOM operates in waters deeper than 200 m and uses atmospheric forcing from the Navy Operational Global Atmospheric Prediction System (NOGAPS) and assimilation of SST and satellite altimeter data obtained via the NAVOCEANO Altimeter Data Fusion Center.

Appendix B

Freak waves

B.1 Introduction

During the last decade, the phenomenon freak wave has gained much attention. Freak, or rogue waves are usually described as steep and giant waves with a wave height a couple times larger than the significant wave height. They tend to appear from nowhere and are generally inconsistent with the surrounding wave field. Freak waves were first recognized by Draper (1964). Mallory (1974) was the first to discuss the generation of these giant waves in the Agulhas Current. He listed 12 reported hits and observations of giant waves between 1952 and 1973. Kharif and Pelinovsky (2003) believed that more than 22 supercarriers have been lost worldwide due to freak waves between 1969 and 1994. It is obvious that freak waves can be very life-threatening to seafarers.

A unique, generally accepted definition of a freak wave has curiously enough not been established, but there are several possibilities to categorize freak waves. The most simple and widely accepted definition defines a freak wave as a wave having a maximum wave height of at least two times the significant wave height ($H/H_s > 2$) (Mori and Janssen, 2004). Within the linear theory of surface gravity waves, the statistical characteristics of waves are consistent with a Gaussian distribution for the instantaneous surface elevation and the Raleigh distribution for the individual wave heights. According to this theory the above criterion of a freak wave would imply that freak waves are expected to occur approximately once every 10^4 waves. It is therefore questionable whether this criterion serves as a good measure for defining such a freakish event. Liu and MacHutchon (2006) examined six years of wave measurements (a total record of 50359 hours) from a gas drilling platform in the South Indian Ocean and found that 1563 potential freak waves within the above criterion, which corresponds with the Raleigh distribution. They proposed another criterion, wherein the term 'freak' is possibly more suitable. Within a total of 50359 hours of measurements, they found 15 cases where $H/H_s > 4$, which implies an occurrence rate of

once every 10^{-8} waves. Such an occurrence rate would certainly befit the nature of rareness by which freak waves are known.

On the other hand, several numerical simulations by Marthinsen and Winterstein (1992) and Forristall (2000) show that the Raleigh distribution for the individual wave heights is somewhat underpredicted. Their models suggest that, especially for the upper tail of the wave height distribution, the extreme waves have a much higher probability. These simulations show good agreement with observed data (Onorato *et al.*, 2005; Dysthe *et al.*, 2008). Several mechanisms to produce extreme waves from moderately small ones are given below.

1. **Spatial focusing**

   Spatial focusing, or refraction, occurs in shallow water areas with varying bottom topography or in variable currents. As waves propagate into shallow water, they align their crests with the topography and steepen. The changing wave direction is due to variations in the phase speed along the wave crest. Along coasts, refraction leads to the local focusing of wave energy. As waves propagate against a current, they can get trapped in the flow, as described in Appendix A.2. Current-induced refraction has been one of the most important mechanisms for generating giant waves (Gründlingh, 1994; Lavrenov, 1998).

2. **Dispersive focusing**

   Due to the effect of dispersion (velocity is inversely proportional to wave frequency), wave energy can be focused into one giant wave when all wave components of a wave train have the right initial phase. Longuet-Higgins (1974) was the first who suggested that when a wave group with a linearly decreasing frequency is properly designed, dispersion forces this group to contract to only a few wavelengths. Dispersive focusing has been examined in wave tanks, but has never been recorded for the ocean (Dysthe *et al.*, 2008). However, it shows the influence of the initial conditions on the probability of occurrence of a freak wave.

3. **Nonlinear focusing**

   Nonlinear focusing has been proposed as one the mechanisms to generate freak waves. Benjamin and Feir (1967) originally found that a regular periodic wave train can grow unstable to side perturbations (modulations), called the modulation instability. Sidebands $\Delta\omega \pm \omega$ grow according to $\Delta\omega / \omega < ak\sqrt{2}$, in which a is amplitude and k is wavenumber. This means that as the instability develops into groups with time scale $(ak)^{-2}$ wave periods, a wave train disintegrates into groups and produces large, isolated waves, see Figure B.1 (Dysthe *et al.*, 2008). Within these groups, nonlinear focusing takes place, producing one extreme wave and several

smaller waves. This mechanism has been verified numerically (Lake *et al.*, 1977; Zakharov, 2006) and experimentally (Tulin and Waseda, 1999) in wave tanks.

This Appendix describes the latter mechanism for the generation of freak waves more extensively, since this effect could also be important in the Agulhas Current region. The next paragraphs will describe the Benjamin-Feir (BF) instability, will introduce the BF Index developed by Janssen (2003) and will further elaborate nonlinear focusing at sea.

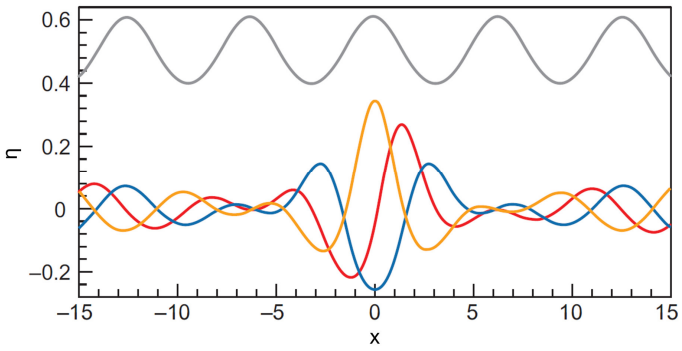

Figure B.1: Development of a freak wave due to nonlinear focusing. A regular wave train (top) develops into an extreme group (bottom), of which three snapshots are shown. Figure by Dysthe *et al.* (2008).

B.2 The Benjamin-Feir Index (BFI) and freak waves

With many applications in plasma physics, optics and water waves, the nonlinear Schrödinger equation (NLS) describes the evolution of an envelope of modulated wave groups. Zakharov (1968) shows that for slowly modulating wave groups, the wave amplitude satisfies the NLS. Janssen (2003) used the Zakharov equation to show that near-resonant wave-wave interactions play an important role in the evolution of the spectrum of surface gravity waves, which he relates to the formation of freak waves. The NLS is valid for unidirectional, weakly nonlinear and dispersive deep water waves and is in its general form described by

$$i\frac{\partial}{\partial t}\psi - \frac{\partial^2}{\partial x^2}\psi - \kappa|\psi|^2\,\psi = 0\,, \tag{B.1}$$

which is related to the amplitude and the phase for the complex field ψ. In deep water, the nonlinearity parameter κ is positive, and thus envelope solutions can occur.

Equation (B.1) can be rewritten as

$$\frac{\partial}{\partial t}a - i\frac{\partial^2}{\partial x^2}a - i\left(\frac{\sqrt{2}\varepsilon}{\Delta K\,/\,k_0}\right)|a|^2\,a = 0\,, \tag{B.2}$$

in which a is the wave envelope of the free surface, $\varepsilon = k_0 a_0$ is the wave steepness of the wave envelope, ΔK is the spectral bandwidth of the wavenumber spectrum and k_0 is the envelope wave number. The nonlinearity parameter κ is described by the term between the brackets in equation (B.2). This amplification factor is known as the Benjamin-Feir instability parameter *or* the Benjamin-Feir Index (*BFI*, Janssen, 2003) and this nonlinear focusing mechanism can result in an amplification of 4.5 – 5 times the initial wave height (Dysthe *et al.*, 2003). Instability occurs if the *BFI* is larger than 1;

$$BFI = \frac{\sqrt{2}\varepsilon}{\Delta K\,/\,k_0} > 1\,. \tag{B.3}$$

The factor $\sqrt{2}$ is included for a random wave train to become unstable if $BFI > 1$. This criterion is also valid for realistic narrow-banded gravity wave spectra. With the average wave steepness for a Gaussian-shaped spectrum $\varepsilon = k_0 m_0^{\frac{1}{2}}$ and with $\Delta K\,/\,k_0 = \sigma_\omega\,/\,\omega_0 = \sigma_\omega^{'} = \left(\sqrt{\pi}Q_p\right)^{-1}$ in terms of Goda's peakedness parameter, this leads to the definition of the *BFI;*

$$BFI = \sqrt{2\pi}Q_p\varepsilon\,. \tag{B.4}$$

Essentially the *BFI* is the ratio of the dispersion and the nonlinearity of the waves *or* the ratio of the average steepness of the wave and their degree of randomness. Again assuming a Gaussian shaped spectrum in a narrow-band approximation, Mori and Janssen (2004) found that the fourth order cumulant of the surface elevation κ_{40} depends on the square of the *BFI*;

$$\kappa_{40} = \frac{\pi}{\sqrt{3}}BFI^2\,. \tag{B.5}$$

This cumulant equals the kurtosis (or peakedness of the spectrum) minus three. Mori and Janssen (2004) found that for a narrow-band, random wave train, the wave height and the maximum wave height probability distribution depend on the wave variance and this kurtosis. The original approach of wave statistics (Raleigh distribution) ignored this effect. According to the original wave statistics, the wave height exceedance probability for a random wave field is expressed in terms of a Weibull distribution, where

$$P(H > \gamma H_s) = \exp(-\gamma^\alpha\,/\,\beta)\,, \tag{B.6}$$

for which Longuet-Higgins (1952) found $\alpha = 2$ and $\beta = 0.5$ for a linear, narrow-banded wave field. Including the effect of the kurtosis, Mori and Janssen (2004) found that for weakly, narrow spectra the probability of a wave height exceeding γH_s can be described by the Edgeworth distribution:

$$P(H > \gamma H_s) = \exp(-2\gamma^2)\left[1 + \kappa_{40}\left(2\gamma^2\left(\gamma^2 - 1\right)\right)\right]. \tag{B.7}$$

From (B.7) it follows that for $BFI > 0$ the probability of encountering a freak wave is higher, due to nonlinear focusing (see also Figure B.2).

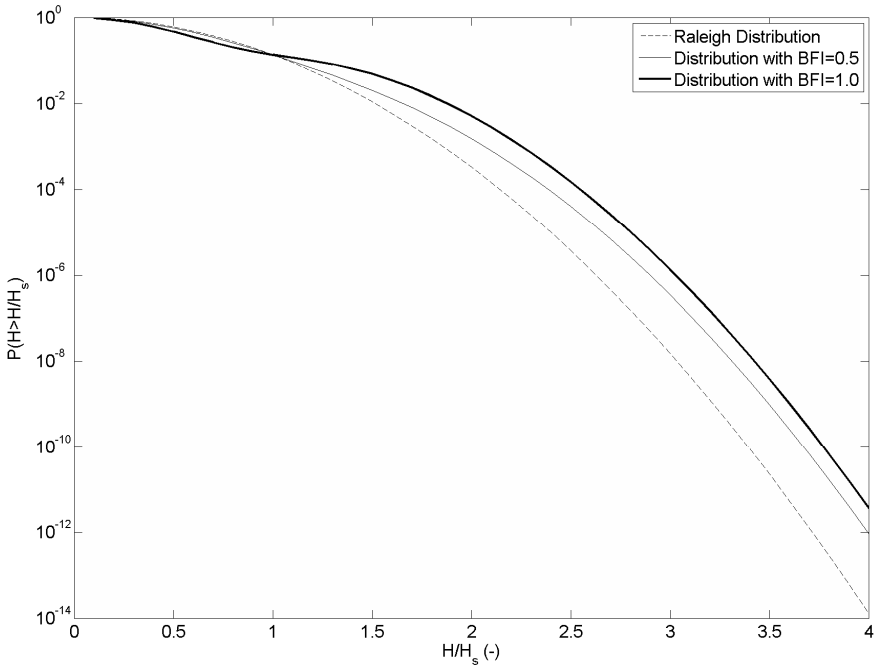

Figure B.2: Raleigh distribution and the wave height probability distributions with $BFI = 0.5$ and $BFI = 1$.

As follows from Figure B.2, the *BFI* can be described as a correction to the Raleigh distribution. These results have been verified by large-scale wave tanks experiments (Onorato *et al.*, 2005; Mori and Janssen, 2004) with unidirectional waves and the distributions with the included *BFI* well predict the spatial development of the kurtosis, the wave height distribution and the maximum wave height distribution in the wave tanks (Mori *et al.*, 2007). However, several numerical simulations (Dysthe *et al.*, 2003; Socquet-Juglard *et al.*, 2005; Onorato *et al.*, 2006) and wave tank experiments (Waseda *et al.*, 2006; Mori *et al.*, 2009) show that not only the BFI has an influence on the kurtosis, but also the directional dispersion. The results show that the directional dispersion effects suppress the kurtosis enhancement in directional sea states (as in the ocean). Equation (B.7) thus needs to be adjusted to include directional effects.

B.3 The BFI and directional effects

As stated earlier, the correspondence of the *BFI* to extreme wave statistics was verified by Onorato *et al.* (2005) for unidirectional waves. However, numerical simulations show that the introduction of directionality of the wave spectrum considerably reduces the extreme wave occurrence. In a wave tank experiment, Waseda (2006) used a frequency spectrum of the JONSWAP type, discretized into 1024 components conserving energy for each frequency bin. The directional distribution of the Mitsuyasu-type was used:

$$D(\theta) = D_m \cos^m(\theta). \tag{B.8}$$

The directional spreading varied between $m = 1$ to 125 and the frequency spectrum was fixed with a peakedness factor of $\gamma = 3.0$ and $BFI = 0.3152$. Waseda examined waves of H_s = 3.50 cm and H_s = 4.15 cm, which corresponds to a wave steepness of 0.13. In our study, we use the (one-sided) directional width σ_θ instead of m. The directional width as a function of m (Kuik *et al.*, 1988) is:

$$\sigma_\theta^2 = 2 - \left(\frac{2}{\left(\frac{m}{2} + \frac{1}{2}\right)} \cdot \frac{\Gamma^2\left(\frac{m}{2} + 1\right)}{\Gamma^2\left(\frac{m}{2} + \frac{1}{2}\right)} \right), \tag{B.9}$$

where $\Gamma(.)$ is the gamma function (see Figure B.3).

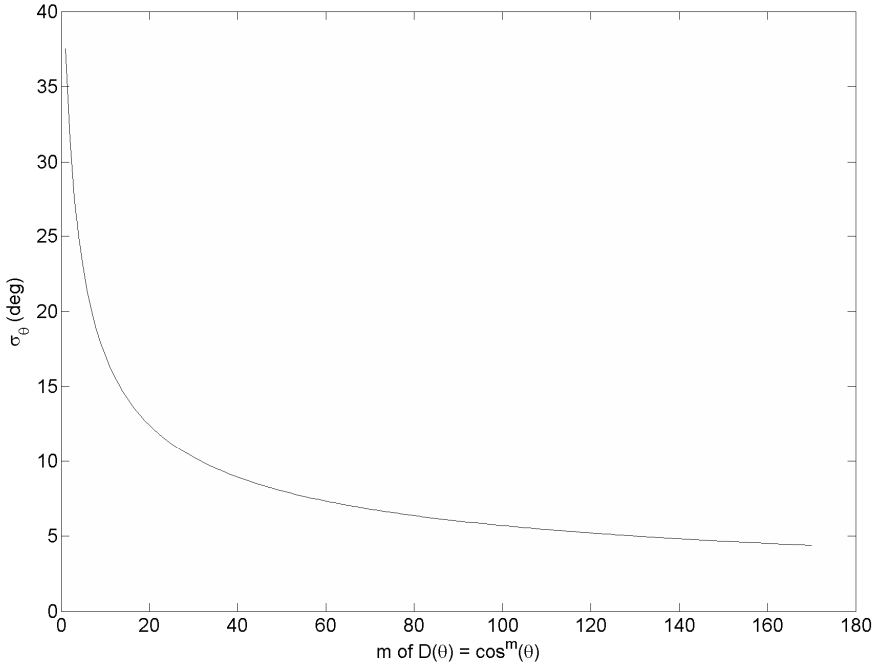

Figure B.3: Relation between m of equation (B.8) and the (one-sided) directional bandwidth.

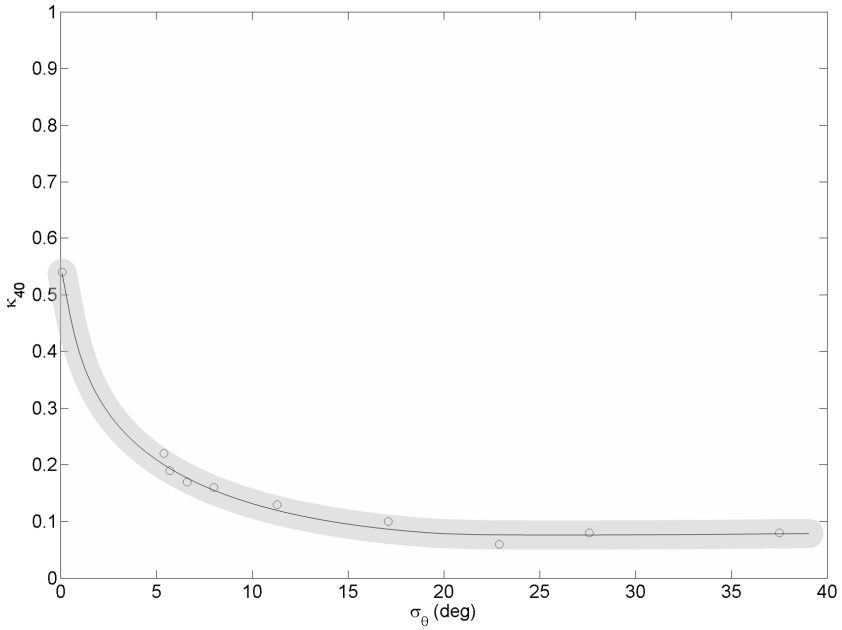

Figure B.4: Kurtosis plotted against directional bandwidth (deg) for $BFI = 0.3152$ in the wave tank experiment of Waseda (2006).

Waseda (2006) observed that for the given *BFI*, the kurtosis takes values between 0.1 and 0.6 and that it reduces as the directional spectrum broadens (see Figure B.4). In the open ocean, a realistic directional spreading is around 30°, so the expected magnitude of the kurtosis is less than 0.1, much smaller than for the unidirectional case, when the kurtosis is about 0.54. This suggests that the relation between kurtosis and *BFI* in equation (B.5) is not complete, thus the theory needs to be extended to include directionality.

Utilizing a directional wave generator in a laboratory wave tank, Waseda *et al.* (2008) found a new relation between the kurtosis and the *BFI* including directional effects. They introduced the *effective BFI* as an extension of the conventional *BFI*. The effective Benjamin-Feir Index BFI_{eff} successfully parameterized the observed occurrence of freak waves in the tank and can be estimated from the directional wave spectrum (Waseda *et al.*, 2008) as

$$BFI_{eff} = \frac{\varepsilon_{eff}}{\sqrt{(\delta k/k)^2 - 2(\delta l/k)^2}}, \tag{B.10}$$

in which (dk,dl) is the perturbation wavenumber. In contrary to the *BFI*, this dimensionless index takes into consideration the newly introduced effective spectral bandwidth $\sqrt{(\delta k/k)^2 - 2(\delta l/k)^2}$ and the corresponding effective steepness ε_{eff} (Waseda *et al.*, 2008).

The first term $\delta k/k$ can be estimated using Goda's parameter (the width of the wave spectrum) with

$$\delta k/k = a\left(\frac{0.69}{Q_p} - 0.01\right), \tag{B.11}$$

in which $a = 1.1/\sqrt{2}$. Goda's parameter Q_p is defined as

$$Q_p = 2\frac{\iint \sigma E^2(\sigma,\theta)\,d\sigma d\theta}{\left(\iint E(\sigma,\theta)\,d\sigma d\theta\right)^2}. \tag{B.12}$$

The second term $\delta l/k$ can be estimated using the normalization coefficient A in the directional distribution $D(\sigma,\theta)$ (Holthuijsen, 2007), for which holds that (see also Figure B.5)

$$D(\sigma,\theta) = A\cos^m\theta; \text{ and } A = \left(\Gamma\left(\tfrac{m}{2}+1\right)/\Gamma\left(\tfrac{m}{2}+\tfrac{1}{2}\right)\right)/\sqrt{\pi}\,. \tag{B.13}$$

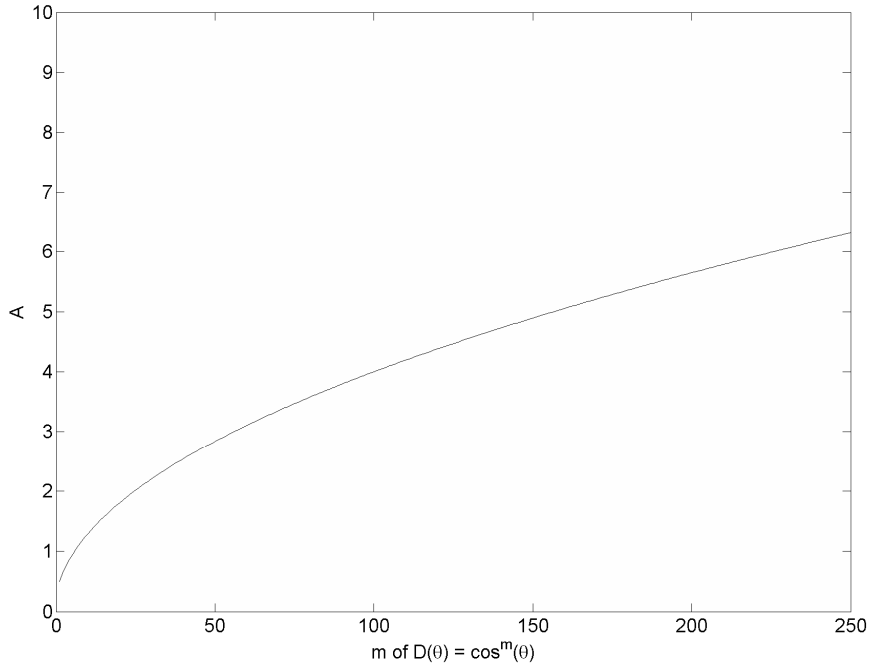

Figure B.5: Relation directional distribution parameter A and m according to equation (B.13).

$\delta l/k$ is now estimated as

$$\delta l / k = b\left(\frac{0.82}{A} - 0.11\right), \tag{B.14}$$

in which $b = 0.45/\sqrt{2}$. The effective steepness ε_{eff} can be estimated as

$$\varepsilon_{eff} = \varepsilon\sqrt{1 - \delta\kappa / 4 - (5/8)\delta\kappa^2}\,, \tag{B.15}$$

where ε is the steepness from the spectrum, and $\delta\kappa = \sqrt{\delta k^2 + \delta l^2}$. Combining (B.11), (B.14) and (B.15) leads to the formulation of the *effective BFI* of equation (B.10). The kurtosis does not monotonically increase with BFI_{eff}, see Figure B.6.

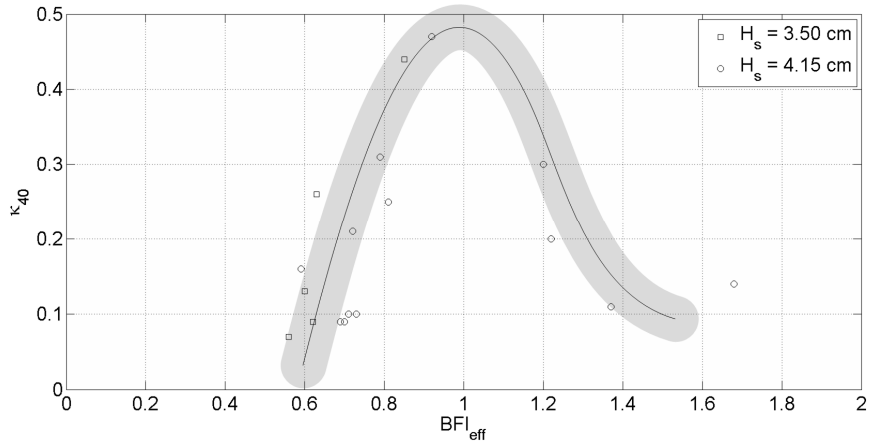

Figure B.6: Kurtosis plotted against the *effective BFI* in a wave tank experiment (Waseda, 2008).

From the wave tank experiment, Waseda *et al.* (2008) found a maximum kurtosis of 0.5 for $BFI_{eff} = 1$ and decreasing values for $BFI_{eff} > 1$ and $BFI_{eff} < 1$ for rather narrow directional distributions (with a spreading of 20° and less). From equation (B.10) it follows that to obtain real values for the BFI_{eff}

$$(\delta k / k)^2 \geq 2(\delta l / k)^2, \tag{B.16}$$

which is only true for relatively small values for Q_p (relatively wide spectrum, and thus a high degree of randomness) and/or relatively large values for A (narrow directional distribution). For the Agulhas Current, we found values for Q_p between 1.5 and 3 (in a following current and in an opposite current respectively), and values for A between 0.45 and 0.65 (corresponding to 40° and 30° directional spreading, respectively), thus resulting in values of $(\delta k / k)^2$ between 0.03 and 0.12, and $(\delta l / k)^2$ between 0.14 and 0.24. For such a

sea state with a directional spreading of about 30° or larger, the criterion (B.16) is therefore never met.

Another study by Mori *et al.* (2009) showed similar results. To include the directional dispersion effects in (B.7), Mori *et al.* (2009) used Monte Carlo simulations with the nonlinear Schrödinger equation (MCNLS) and estimated the kurtosis for the directional sea states. They found that the kurtosis is proportional to the inverse of the directional spectrum bandwidth. They showed that the results of the MCNLS can be described using: (see also Figure B.7)

$$\kappa_{40} = \left(\frac{\pi}{\sqrt{3}}\right) BFI^2 \left(\frac{1}{1 + b\sigma_\theta}\right)^c , \tag{B.17}$$

where κ_{40} and σ_θ(rad) are the kurtosis of the surface elevation and the directional spreading, respectively. The empirical coefficients $b = 7.68$ and $c = 2.06$ were estimated by the least-square method (Mori, 2009). In contrary to the findings by Waseda *et al.* (2008), equation (B.17) has solutions for any value of σ_θ and *BFI*.

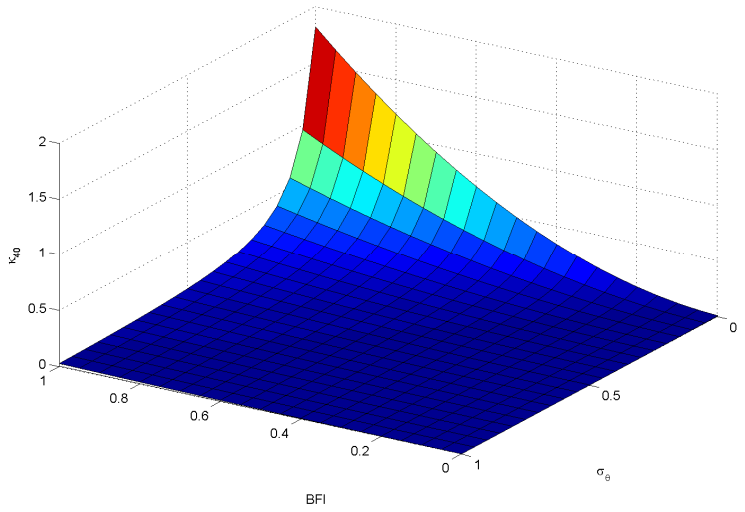

Figure B.7: Kurtosis dependence on *BFI* and σ_θ according to equation (B.17).

From (B.17) and Figure B.7 it becomes clear that the effect of including the directional spreading is enormous. For a typical wind sea with a directional spreading of $\sigma_\theta = 0.5$ (approximately 30°), the effect of the *BFI* on the kurtosis is almost zero.

To demonstrate this, we computed the *BFI* in the Agulhas Current, see Figure B.8. The maximum calculated $BFI = 0.62$ in the anticyclonic ring (near 12°E; 41°S) resulted in a maximum value for the kurtosis $\kappa_{40} = 0.70$ without including directional effects. According to equation (B.7), the exceedance probability of encountering a freak wave with $H/H_s > 2$ would then be increased by a factor 18, compared to the Raleigh distribution. The directional spreading at this location was $\sigma_\theta = 0.63$. Including this in (B.17), the kurtosis would be reduced by a factor 35 to $\kappa_{40} = 0.02$. This result suggests that the exceedance probability of encountering a freak wave within the same criterion as above would be increased only by a factor 1.5. With $BFI = 0.40$ and $\sigma_\theta = 0.54$ outside the current, the kurtosis is $\kappa_{40} = 0.01$, thus implying again that the conditions for a relatively larger occurrence of freak waves are extremely rare.

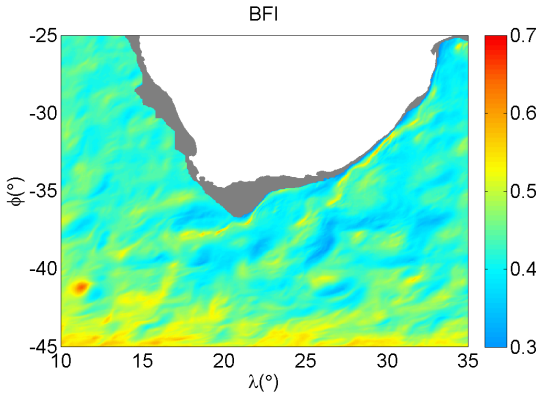

Figure B.8: Geographic distribution of the BFI in and near the Agulhas Current for a uniform wind (U_{10} = 15 m s^{-1} from 45°, Cartesian) and a uniform wave boundary condition (significant wave height of H_s = 3.0 m and a peak period of T_p = 7.0 sec, propagating in the same direction as the wind) using the WRT method.

B.4 Conclusions

The numerous reports and stories about giant freak waves in the ocean have resulted in many freak wave studies trying to understand the mechanisms of freak wave generation. Three main mechanisms can be distinguished; spatial focusing, dispersive focusing and nonlinear focusing. Currently, the latter mechanism is the most active research topic and is studied theoretically, numerically and experimentally (in wave tanks), in the hope that it might provide the key to forecasting the occurrence of freak waves. As was discussed in this appendix, the wave height probability distribution according to the original wave statistics of Longuet-Higgins (1957) can be described using the Raleigh distribution. However, numerical simulations, verified with experimental results show that the probability of encountering large waves is a factor higher. This factor can be described with relation to the

kurtosis (or peakedness of the wave spectrum), which proved to be related to the *BFI*, an index to quantify the Benjamin-Feir instability. Recent research has shown that the relation between *BFI* and kurtosis needed to be extended to include directional effects. These results led to new formulations of the *BFI*, introduced as a new parameter, called the effective *BFI*. We showed that the reduction of the kurtosis is monotonic as the directional spreading increases. For a typical wind sea with a directional spreading around 30°, the effect on the kurtosis and thus the occurrence of freak waves is almost zero. With the directional effects included, an increase of kurtosis is thus extremely rare and can only occur when the spectral directionality is narrow, see Figure B.7. The next step is now to find out when and how often such conditions occur at sea. Tamura *et al.* (2009) recently suggested that a narrow wave spectrum may develop in realistic sea states where swells and wind sea coexist and that this is perhaps the key for understanding freak wave generation due to nonlinear focusing at sea. A careful and quantitative validation in the field will thus be required in the near future.

Appendix C

Model convergence

When implementing SWAN in a specific site the simplest way would be to use the default mode. However, better results can be obtained by activating alternative formulations for the key processes. This appendix describes three available whitecapping formulations, namely:

1) Komen's *et al.* (1984) parameterization to describe the transfer of wind energy to the waves coupled with the pressure pulse based model of Hasselmann (1974) for whitecapping dissipation.
2) Yan's (1987) model for atmospheric input coupled with the saturation based model of Alves and Banner (2003) for whitecapping.
3) Komen's *et al.* (1984) parameterization coupled with the bore-based model of Battjes and Janssen (1978) for whitecapping dissipation.

C.1 Pressure pulse based whitecapping

The default option in SWAN is to use the exponential wind growth formulation and the whitecapping formulation of Komen *et al.* (1984), based upon the theory of Hasselmann (1974). Hasselmann describes each white-cap as a pressure pulse that acts on the sea surface, just downwind of the wave crest. At that location in the wave, the weight of the white-cap acts against the rising sea surface, thus draining energy from that wave (energy dissipation). The source term for the dissipation due to whitecapping can be written as

$$S_{wcap}(\sigma,\theta) = -\Gamma_{KJ}\tilde{\sigma}\frac{k}{\tilde{k}}E(\sigma,\theta)\,, \tag{C.1}$$

in which $\tilde{\sigma}$ and $\tilde{k}$ are the mean frequency and the mean wave number, respectively, and the coefficient Γ_{KJ} depends on the overall wave steepness. The steepness coefficient Γ_{KJ} can be written as:

$$\Gamma_{KJ} = C_{ds}\left(\frac{\varepsilon}{\tilde{\varepsilon}_{PM}}\right)^4. \tag{C.2}$$

The coefficient C_{ds} is 2.36×10^{-5}, s the wave steepness, defined as $\varepsilon = \tilde{k}\sqrt{E_{tot}}$, and ε_{PM} is the overall steepness of the Pierson-Moskowitz spectrum, $\varepsilon_{PM} = 5.4955 \times 10^{-3}$.

For the Agulhas Current, the default model proved not stable and did not converge, see Figure C.1. We show this for one particular point (18°E; 40°S) in the current with 60 iterations. It is shown that the generation by wind and the quadruplet wave-wave interactions have converted, whereas all other wave parameters have not.

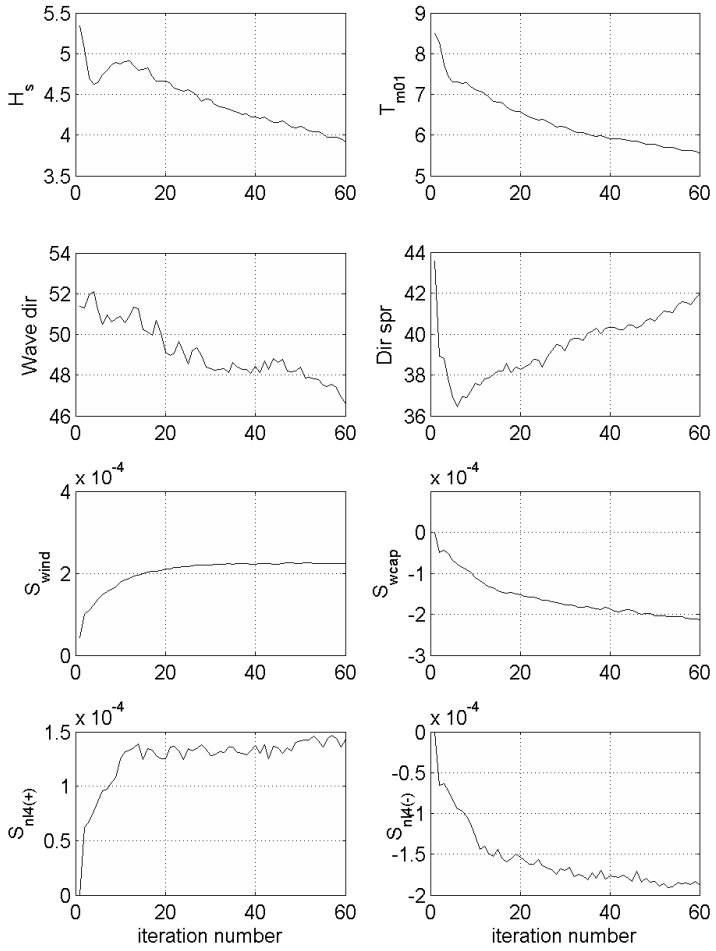

Figure C.1: Convergence of the significant wave height H_s (m), relative mean wave period T_{m01} (s), wave direction (°, Cartesian), directional spreading (°) and the source terms generation by wind, whitecapping dissipation and quadruplet wave-wave interactions using the formulation of Komen (1984) and the DIA method for quadruplet wave-wave interactions at 18°E; 40°S in the Agulhas Current.

C.2 Saturation based whitecapping

Another formulation is Yan's (1987) model for the wind input coupled with the saturation based model of Alves and Banner (2003). The latter model is based on the relationship between wave groups and whitecapping dissipation, where:

$$S_{wcap}(\sigma,\theta) = C_{ds}\left(\frac{B(k)}{B_r}\right)^{p/2}(\tanh(kh))^{(2-p_0)/4}\sqrt{gk}\cdot E(\sigma,\theta)\,. \tag{C.3}$$

The expression for exponential growth by wind (Komen *et al.*, 1984) is a function of u_*/c:

$$S_{wind}(\sigma,\theta) = \beta E(\sigma,\theta), \text{ with } \beta = \max\left[0, 0.25\frac{\rho_a}{\rho_w}\left(28\frac{u_*}{c}\cos(\theta-\theta_w)-1\right)\right]\sigma \tag{C.4}$$

in which ρ_a and ρ_w are the density of air and water, respectively, u_* is the friction velocity of the wind and c the phase velocity of the waves. The basic principle of the wind input expression of Yan (1987) is that for strong winds (i.e. $u_*/c > 0.1$), the wind-induced growth rate of waves depends quadratically on u_*/c, whereas for weaker winds, the growth rate depends linearly on u_*/c. Yan (1987) proposed an analytical fit through these two ranges. The difference between the wind input by Komen *et al.* (1984) and Yan (1987) is given in Figure C.2 in terms of the coefficient β of wind-induced wave growth.

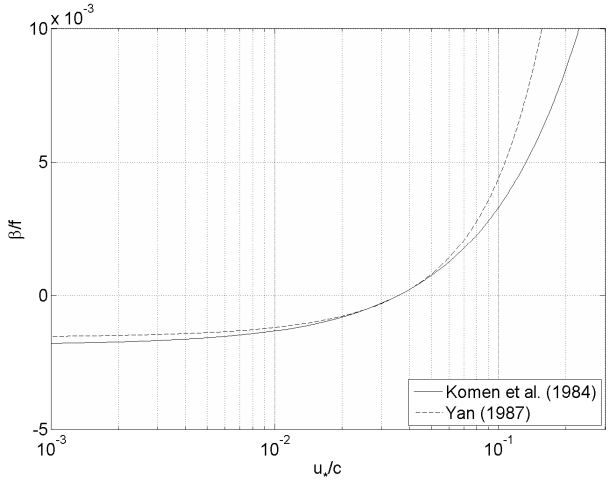

Figure C.2: The coefficient of the wind-induced wave growth for the wind growth formulation of Komen *et al.* (1984) and Yan (1987).

For the Agulhas Current, the default model proved not stable and did not converge, see Figure C.1. We show this for one particular point (18°E; 40°S) in the current with 60 iterations. It is shown that the generation by wind and the quadruplet wave-wave interactions have converted, whereas all other wave parameters have not.

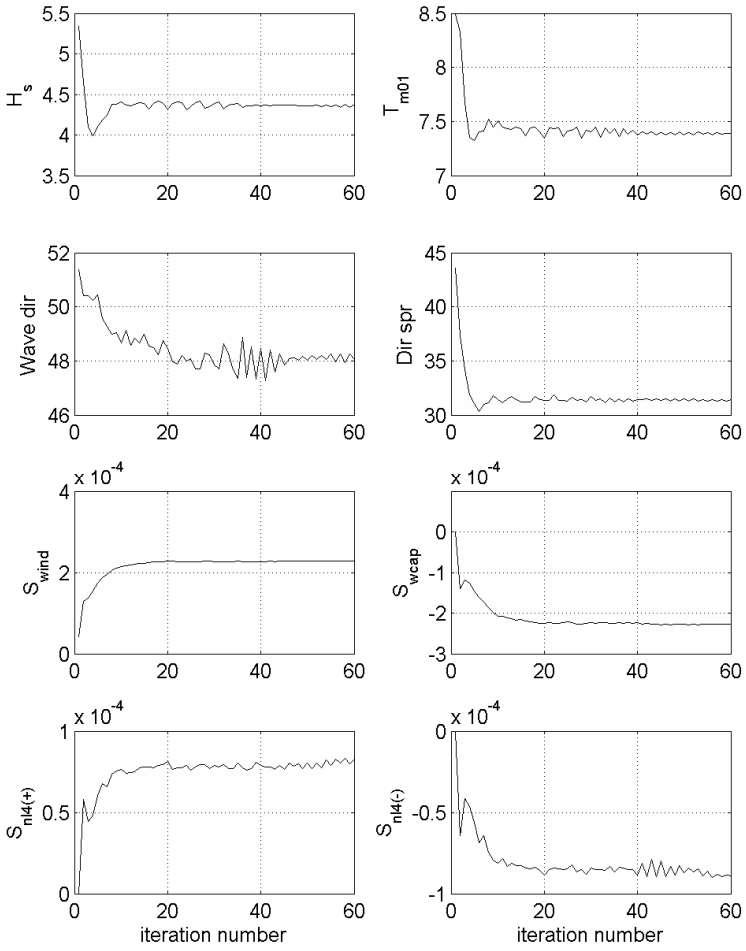

Figure C.3: Convergence of the significant wave height H_s (m), relative mean wave period T_{m01} (s), wave direction (°, Cartesian), directional spreading (°) and the source terms generation by wind, whitecapping dissipation and quadruplet wave-wave interactions using Yan (1987) for wind input and Alves and Banner (2003) for whitecapping dissipation and the DIA method for quadruplet wave-wave interactions at 18°E; 40°S in the Agulhas Current.

When the nonlinear saturation based model for whitecapping is used in combination with the wind input by Yan (1987), the convergence is much more promising compared to the formulations by Komen *et al.* (1984), see Figure C.3. After about 20 iterations all variables seem to have been converted to a solution. The convergence of wave direction shows jumps around iteration 40, but it equilibrium remains around 48°.

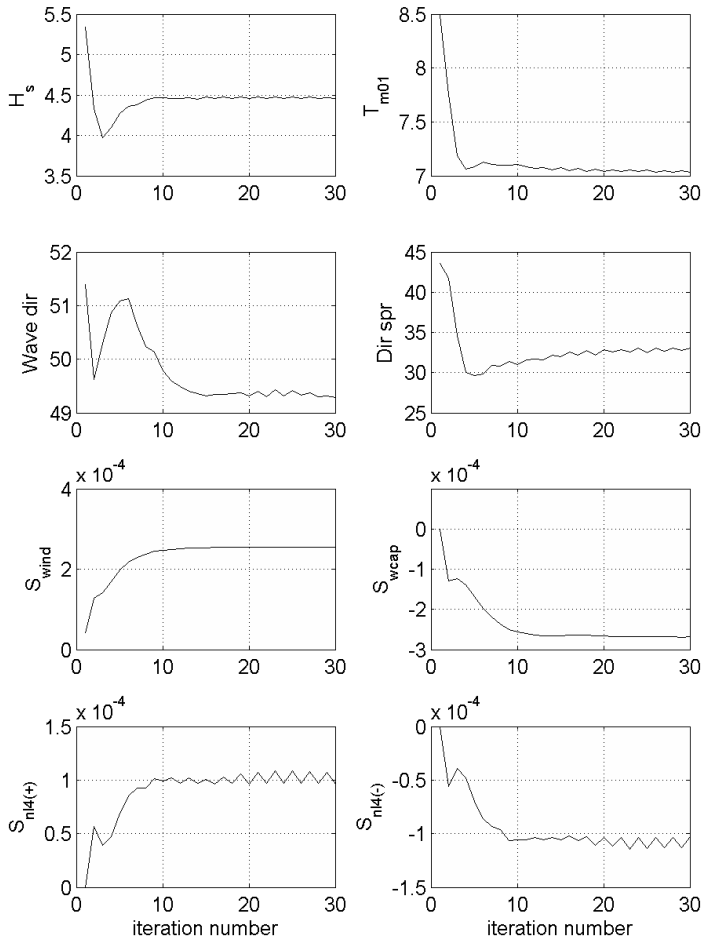

Figure C.4: Convergence of the significant wave height Hs (m), relative mean wave period Tm01 (s), wave direction (°, Cartesian), directional spreading (°) and the source terms generation by wind, whitecapping dissipation and quadruplet wave-wave interactions using Yan (1987) for wind input and Alves and Banner (2003) for whitecapping dissipation and the WRT method for quadruplet wave-wave interactions at 18°E; 40°S in the Agulhas Current.

In our study, we used the WRT method for the computation of quadruplet wave-wave interactions (see also next appendix). For the Agulhas Current, we found that the saturation based model in combination with the WRT method converged as well, see Figure C.4. We therefore used this model in all of our computations.

C.3 Bore based whitecapping

Ris and Holthuijsen (1996) proposed a third method. They studied the performance in SWAN in situations of wave blocking in countercurrents (see also appendix A.2) and proposed a method based on the parameterization of Komen *et al.* (1984) for wind input and the bore-based model of Battjes and Janssen (1978) for whitecapping dissipation. Within the latter model, the steepness coefficient can be written as

$$\Gamma_{BJK} = \frac{\alpha_{BJ} H_{\max}^2 Q_b}{\pi H_{\text{rms}}^2}\,, \tag{C.5}$$

in which Q_b is the fraction of breakers and,

$$H_{\max} = \frac{\varepsilon_{BJ}}{\tilde{k}} \tag{C.6}$$

in which ε_{BJ} is the value for the steepness and $\tilde{k}$ is the mean wavenumber. It is not mentioned in the SWAN manual (Holthuijsen *et al*, 2008), but the option can be used with the following command:

```
WCAPping KBJ [bjstp] [bjalf] [kconv]
```

The value for `[bjstp]` is the steepness ε_{BJ}, set to 0.88 (Miche's criterion of maximum steepness), `[bjalf]` the value for α_{BJ} and is set to 1, and `[kconv]` $= \sqrt{(k/\tilde{k})^3}$, set to 1 (see Lansen, 2006). Ris and Holthuijsen (1996) found that wave blocking can occur in strong countercurrents and that the formulation by Battjes and Janssen (1978) for whitecapping dissipation in SWAN can give reasonable results. However, in the Agulhas Current, wave blocking only occurs in very moderate wave climates. Wave blocking occurs when the current velocity is larger and opposite to the local group velocity ($U > c_g$). With $c_g = g/4\pi\sigma$ and maximum velocities of $U = 2.0$ m s^{-1} in the coastal jet, wave blocking can only occur for very short waves with frequencies $\sigma > 0.40$ Hz. With our conditions considerable wave heights and current gradients, the modified whitecapping model of Battjes and Janssen (1978) will thus not have a considerable influence on the steepness compared to the default model of Komen *et al.* (1984), and we will therefore not use this model in our study.

Appendix D

Exact Quadruplet interaction

Wave growth in deep water is affected by the generation of wind, whitecapping dissipation (discussed in the previous appendix) and the transfer of energy by resonance amongst wave components. The latter process is the quadruplet wave-wave interaction and is briefly described in this appendix. Since exact computations of quadruplet wave-wave interaction are extremely demanding in terms of computer requirements, the default SWAN model uses the DIA approximation for computing these quadruplet wave-wave interactions. However, the DIA is a poor approximation regarding directionality, especially for long-crested waves. As described in appendix B, the directional spreading tends to be important regarding wave enhancement and freak wave occurrence. In our study, the computation of the quadruplet wave-wave interactions could therefore be important in the evolution of the wave spectrum. A near-exact method - the WRT method after Webb (1978), Tracy and Resio (1982) and Resio and Perrie (1991) - was implemented in SWAN by Van Vledder (2006), named Xnl. In this appendix we give a brief description of the WRT method and its performance in terms of wave growth, and we compare our results with the DIA in terms of directionality and computational demands.

D.1 The WRT method

Hasselmann (1962) found that in deep water a set of four waves (a quadruplet) could exchange energy amongst each other when the following resonance conditions are satisfied

$$\begin{cases} \sigma_1 + \sigma_2 = \sigma_3 + \sigma_4 \\ \vec{k}_1 + \vec{k}_2 = \vec{k}_3 + \vec{k}_4 \end{cases} \tag{C.7}$$

in which σ_i is the radian frequency and $\vec{k}_i$ the wavenumber vector of the four interacting waves (i = 1,...,4) which are in turn related via the dispersion relation in deep water

$\sigma^2 = gk$. Hasselmann (1962) describes the nonlinear interactions between waves in terms of their action density N. The rate of change of action density at a wavenumber $\vec{k}_i$ due to all quadruplet interactions involving $\vec{k}_i$ is then given by the Boltzmann integral

$$S_{nl4}(\vec{k}_1) = \iiint G(\vec{k}_1,\vec{k}_2,\vec{k}_3,\vec{k}_4)\delta(\vec{k}_1+\vec{k}_2-\vec{k}_3-\vec{k}_4)\delta(\sigma_1+\sigma_2-\sigma_3-\sigma_4) \times[N_1N_2(N_3+N_4)-(N_1+N_2)N_3N_4]\,\mathrm{d}\vec{k}_2\mathrm{d}\vec{k}_3\mathrm{d}\vec{k}_4 \tag{C.8}$$

where $N_i = N(\vec{k}_i)$ is the action density at the wavenumber $\vec{k}_i$, G is the coupling coefficient and δ are the Dirac delta functions which ensure that contributions to the integral only occur for quadruplets satisfying the conditions given by (C.7) (Van Vledder, 2006). Webb (1978) numerically solved the Boltzmann integral by using several analytical transformations and was therefore able to eliminate the delta functions. Tracy and Resio (1982) incorporated this method in a computational model for discrete deep-water spectra. This computational method is generally known as the WRT method. Since in deep water $\sigma^2 = gk$, the resonance conditions (C.7) lead to

$$\begin{cases} \sqrt{k_1}+\sqrt{k_2} = \sqrt{k_3}+\sqrt{k_4} = \alpha\sqrt{k} \\ \vec{k}_1+\vec{k}_2 = \vec{k}_3+\vec{k}_4 = \vec{k} \end{cases} \tag{C.9}$$

For a fixed value of α all sets of wavenumbers satisfying the resonance conditions lie one a specific curve in the interaction diagram, as proposed by Hasselmann (1962), see Figure D.1. Points P and P' in this diagram can move independently along the curve, thus resulting in many wave number resonant configurations (Van Vledder, 2006).

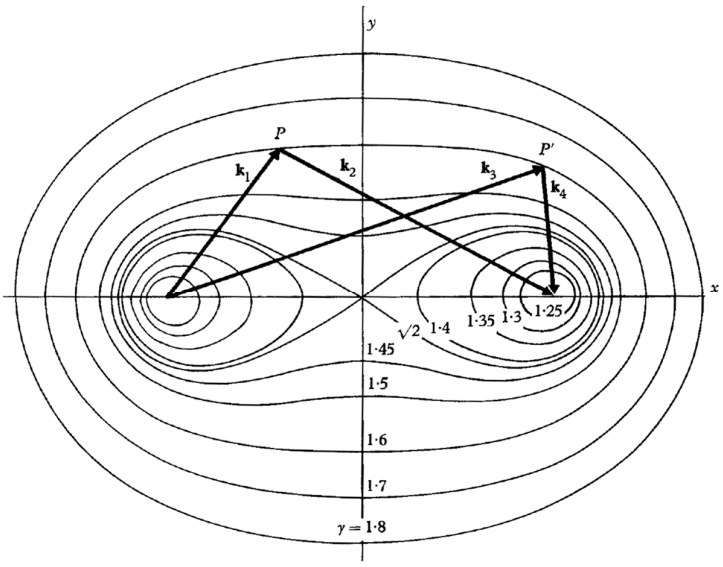

Figure D.1: Interaction diagram (after Phillips, 1957 and Hasselmann, 1962).

For the WRT method, the integration space consists of all possible combinations of resonant quadruplets. The DIA on the other hand, only considers one quadruplet configuration (with $\alpha = \sqrt{2}$) and its mirror image. Compared to the WRT, this implies that only a subset (one point on a curve) of a subset (one curve) of all possible wave number configurations is used, resulting in three to four orders of magnitude less possible configurations. Without a doubt, it can therefore be stated that the DIA is computationally much cheaper than the WRT but also less accurate.

D.2 Wave growth using the WRT method

As we already mentioned in appendix C, in our study we found that the default (pressure pulse based) model (Komen *et al.*, 1984) for whitecapping dissipation in SWAN did not converge, whereas the saturation based model (Van der Westhuysen, 2007) did. In this section we show that the latter model combined with the WRT method not only proves to be stable, but also produces better growth curves when compared to the observations by Pierson and Moskowitz (1964) for a developed sea state and Kahma and Calkoen (1992) for medium fetches. These growth curves are presented using the dimensionless fetch X^*, dimensionless energy ε^* and dimensionless peak frequency σ_p^*:

$$X^* = gX / u_*^2 \; ; \varepsilon^* = g^2 \varepsilon / u_*^4 \; ; \text{and } \sigma_p^* = \sigma_p u_* / g \tag{C.10}$$

Here X is the fetch, ε the total variance of the spectrum, σ_p the peak frequency and u_* the friction velocity. The calibration of the saturation based model for deep water was carried out by Van der Westhuysen (2007) and the curves are presented in Figure D.2. It is shown that the growth curve using the saturation based model combined with the DIA (top row) is less accurate compared to the default model. However, when the saturation based model is combined with the WRT method (bottom row), the growth curve lies well on the observations by Pierson and Moskowitz (1964) and Kahma and Calkoen (1992).

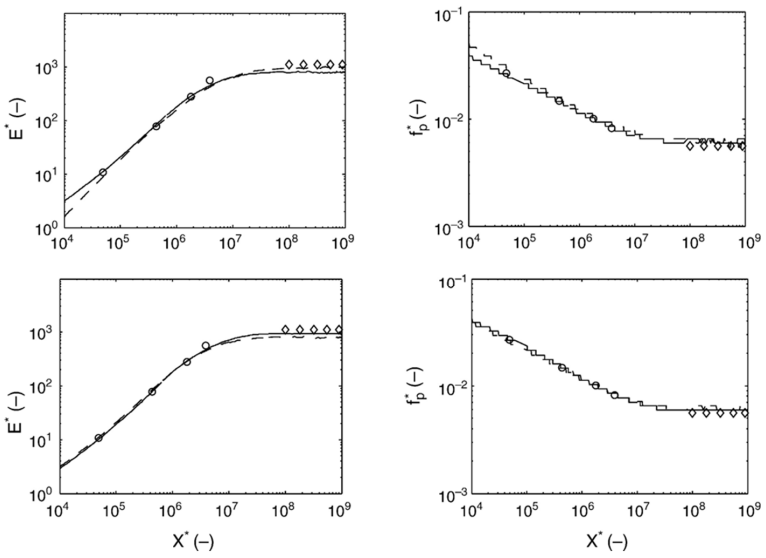

Figure D.2: Deep water, fetch-limited growth curves produced by the saturation-based model (solid lines) and the default model (dashed lines) using the DIA method (top row), and the deep water, fetch-limited growth curves produced by the saturation-based model using the WRT method (solid lines) and the DIA method (dashed lines) (bottom row). Comparison with fetch-limited relations of Kahma and Calkoen (1992) (circles) and Pierson and Moskowitz (1964) (diamonds). Results for $U_{10} = 10$ ms^{-1}.

D.3 Comparison WRT versus DIA in the analytical ring

To show the differences between the default DIA and the WRT method, this section gives an overview of the results of the analytical ring, as described in section 2 of the manuscript, see also Figure 2.3. The results of this particular case show the influences of the different quadruplet interaction methods when waves either follow or counter a current. For this scenario, the directional resolution was 10°, and the frequency resolution was 10%, i.e. $\sigma_{i+1} = 1.1\sigma_i$ with a maximum frequency of 1 Hz. Van Vledder (2006) points out that a sufficiently high maximum frequency is needed in the computations, since interactions with frequencies higher than the maximum frequency are not taken into account. Figure D.3 shows that these cut-off effects do not occur in our case, since the effect vanishes when $\sigma_{\max} > 6\sigma_p$. The nonlinear transfer rate is thus computed for a sufficiently high maximum frequency.

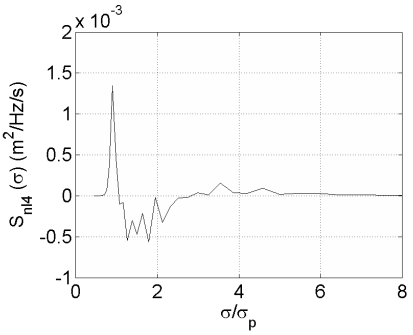

Figure D.3: Non linear transfer rate for the analytical annular current as a function of the normalized frequency $\sigma/\sigma_{\mathrm{p}}$.

For three locations, the directional distributions are presented; in direction of the propagating waves, (1) just before the current at $(x, y) = (0, -150)$, (2) at the maximum countercurrent velocity $(x, y) = (-50, 0)$ and (3) at the maximum following current velocity $(x, y) = (50, 0)$. For each of these locations, the directional distributions using the DIA and the WRT are given for three different frequencies as is shown in respectively Figure D.4, Figure D.5 and Figure D.6. These results show that the directional distributions using the WRT are narrower than when using the DIA for all frequencies.

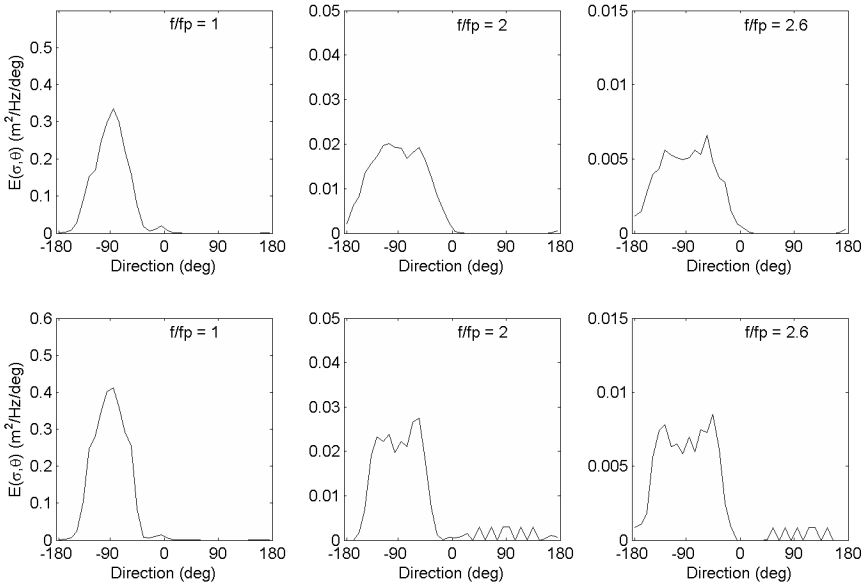

Figure D.4: Directional distributions at the peak and energy-containing tail produced using the DIA (row 1) and the WRT method (row 2) outside the analytical ring.

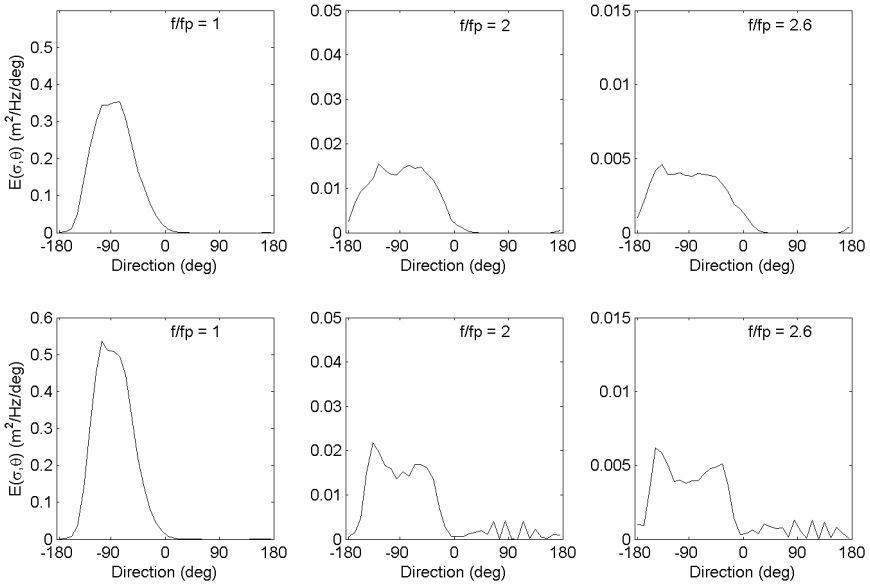

Figure D.5: Directional distributions at the peak and energy-containing tail produced using the DIA (row 1) and the WRT method (row 2) in a countercurrent.

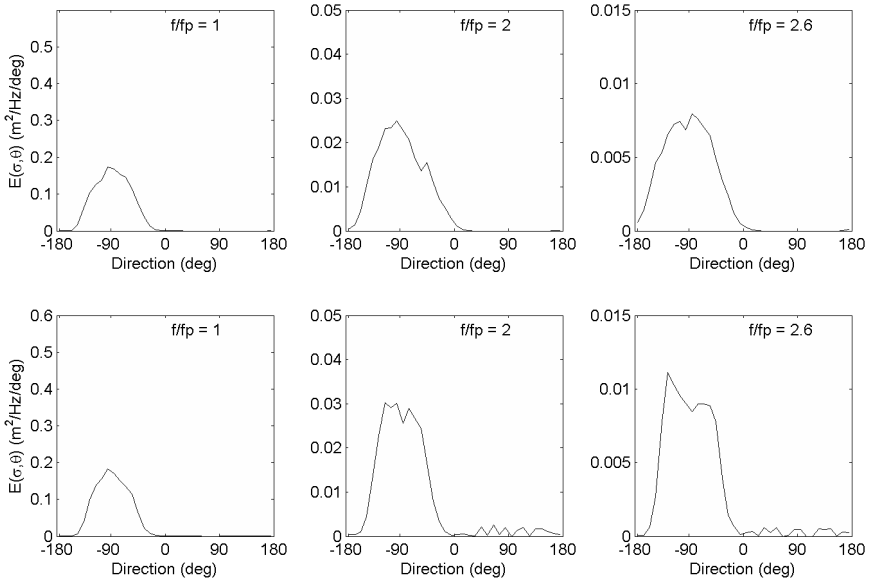

Figure D.6: Directional distributions at the peak and energy-containing tail produced using the DIA (row 1) and the Xnl method (row 2) in a following current.

The WRT method is able to generate a bi-modal distribution (as observed by Hwang *et al.*, 2000) in wave growth situations for frequencies higher than two times the peak frequency, as was also shown by Van der Westhuysen *et al.* (2004). The wiggles at the energy containing tail ($\sigma/\sigma_p > 2$) imply propagating waves against the mean wave direction, which we consider impossible. When these wiggles are removed from the directional distributions (adjusted WRT method), the overall directional spreading decreases with approximately 5°, especially for the higher frequencies, as is shown in Figure D.7. The adjusted directional spreading at each location is given in Figure D.8, which shows a significant increasing directional spreading in a countercurrent and a decreasing spreading in a following current.

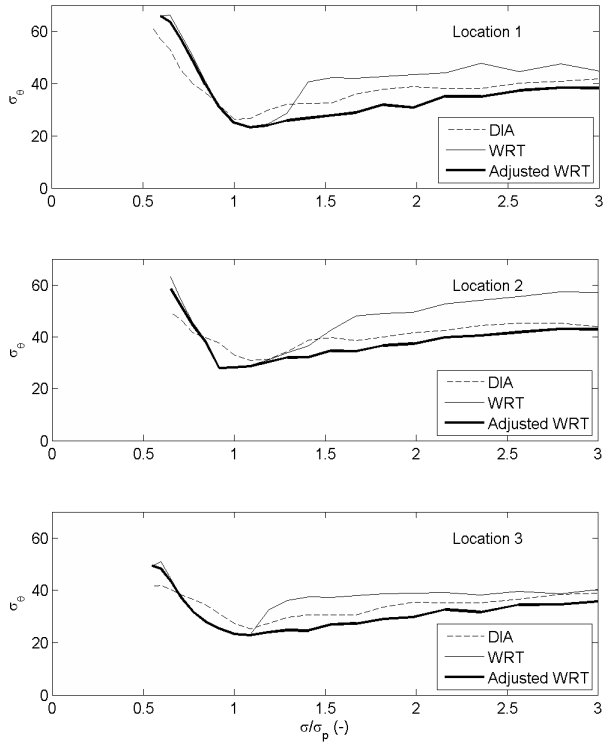

Figure D.7: Directional spreading for the analytical ring using DIA, WRT and the adjusted WRT at three locations; (1) outside the ring, (2) in a countercurrent and (3) in a following current.

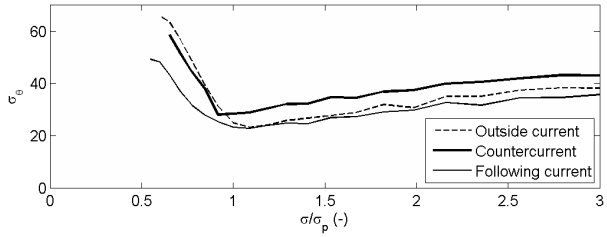

Figure D.8: Directional spreading for the analytical ring using the adjusted WRT at three locations; (1) outside the ring, (2) in a countercurrent and (3) in a following current.

To quantify the effects of the WRT compared to the DIA, we show cross sections of the same characteristic wave parameters (Figure D.9) and geographic distributions of the intensity of the source- and propagation terms (Figure D.10) as were presented in the manuscript. It is shown that the wavelength decreases substantially with about 10% and due to the slightly enhanced refraction the wave heights increase in the ring. As a result, the steepness of the waves increases. This increase means an increase of whitecapping dissipation and enhanced quadruplet wave-wave interactions due to more nonlinear waves. Propagation in geographical space increases in the opposing current, but decreases elsewhere. Furthermore, propagation in frequency space and directional space increase as well.

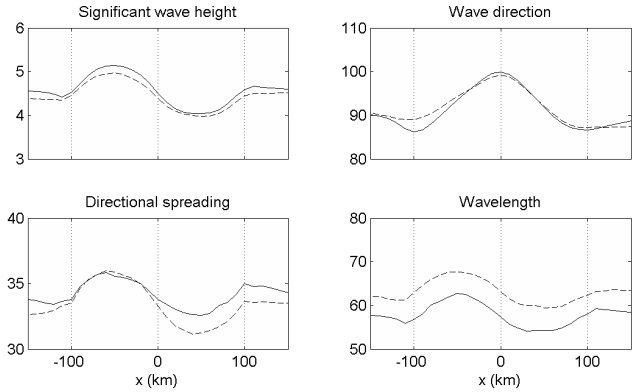

Figure D.9: Cross sections of the geographic distributions of the significant wave height (m) and the wave direction (°, Cartesian) (top row), and the directional spreading (°) and wavelength (m) (bottom row) for the analytical ring using the DIA (dashed line) and the WRT method (solid line).

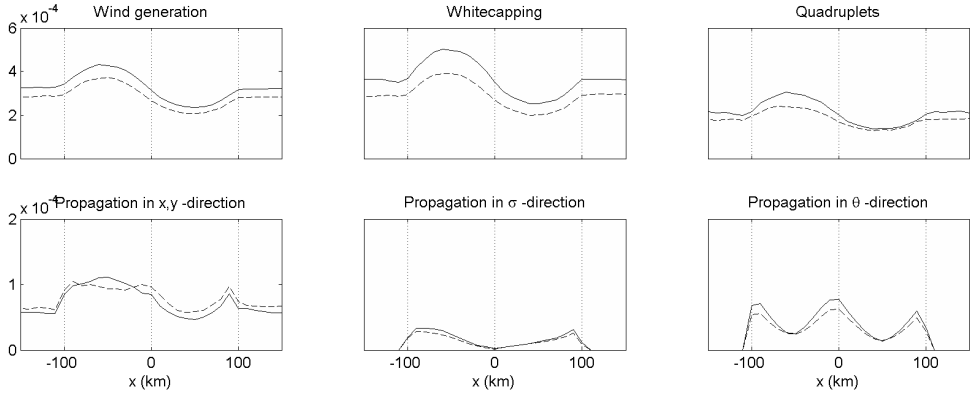

Figure D.10: Cross sections of the geographic distributions of the source terms (top row) and the propagation terms (bottom row) for the analytical ring using the DIA (dashed line) and the WRT method (solid line).

D.4 Computational requirements

Computations using the WRT method demand much more computational time than using the DIA for quadruplet wave-wave interactions. The wave growth simulations and also the three cases drawn out in this study have been computed using both methods. Table D.1, Table D.2 and Table D.3 give the CPU time needed per iteration for each case, whereas the first iteration (first estimate where exact quadruplets are not yet calculated) is discarded. On average, the WRT method demands about 500 times more computational time. Especially for large 2-dimensional runs, the WRT method can at the moment only be used when one has access to large, parallel computer systems.

Table D.1: DIA and WRT computational times for wave growth cases, with U_{10} = 10 m s^{-1}.

Run	*CPU time DIA (sec) Per iteration*	*CPU time WRT (sec) Per iteration*	*Speed difference*
f11grd01	0.28	32.16	115
f11grd02	0.23	29.44	128
f11grd03	2.29	440.23	192
f11grd04	2.29	554.81	242
f11grd05	2.25	582.33	259
f11grd06	7.11	1994.08	281

Table D.2: DIA and WRT computational times for wave growth cases, with U_{10} = 20 m s^{-1}.

Run	*CPU time DIA (sec) Per iteration*	*CPU time WRT (sec) Per iteration*	*Speed difference*
f21grd01	0.24	31.12	130
f21grd02	0.34	28.60	84
f21grd03	1.87	271.98	145
f21grd04	2.22	577.08	260
f21grd05	2.47	717.12	290
f21grd06	5.79	2454.73	424

Table D.3: Computational times for three cases, DIA compared with WRT method, 50 iterations, if only one processor was used.

Run	*CPU time DIA (h)*	*CPU time WRT (h)*	*Speed difference*
Coastal jet	1.2	525	438
Analytical ring	1.5	534	356
Agulhas Current	14.5	10.453	721

Appendix E

Results for the Agulhas Current

This appendix contains several additional results for The Agulhas Current. These results are not useful for publication, but give additional information regarding all processes in the Agulhas Current. The first section gives the one-dimensional wave spectra in and near the Agulhas Current and the second section gives two cross sections of several characteristic wave parameters and the source- and propagation terms in the energy balance equation. The results are computed under the conditions given in section 2 of the manuscript using Yan (1987) for wind input and Alves and Banner (2003) for whitecapping dissipation and the WRT method for quadruplet wave-wave interactions in the Agulhas Current.

E.1 One-dimensional wave spectra

At fifteen locations (indicated in Figure E.1) in and near the Agulhas Current, the one-dimensional spectra are computed. Locations 1 and 6-13 are in the coastal jet along the continental shelf of South-Africa with current velocities opposite to the waves. Locations 2, 14 and 15 are in a following current, location 3 is outside a current and locations 4 and 5 are in the anticyclonic ring in a countercurrent and a following current, respectively. It is shown in Figure E.2 that in a countercurrent, the total energy in the spectrum is increased compared to outside the current (location 3). The opposite effect occurs in a following current. It is also clearly visible that the peak of the spectrum shifts to higher frequencies when waves are in these following currents.

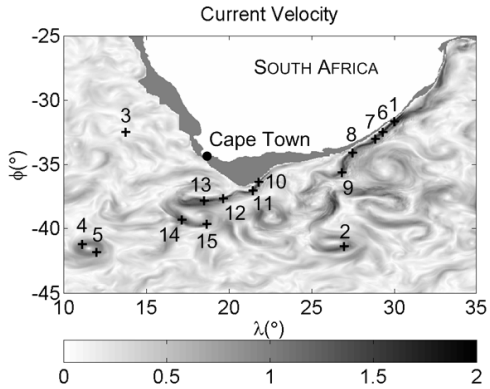

Figure E.1: Current field with velocities (in m s^{-1}) of the Agulhas Current on Oct. 2nd, 2001 from the NLOM ocean model with maximum velocities of about 2.0 m s^{-1} in the coastal jet (between 30° S and 35° S) and 1.0 m s^{-1} in the anticyclonic ring near 12°E; 41°S. At the fifteen locations indicated, one-dimensional spectra will be presented.

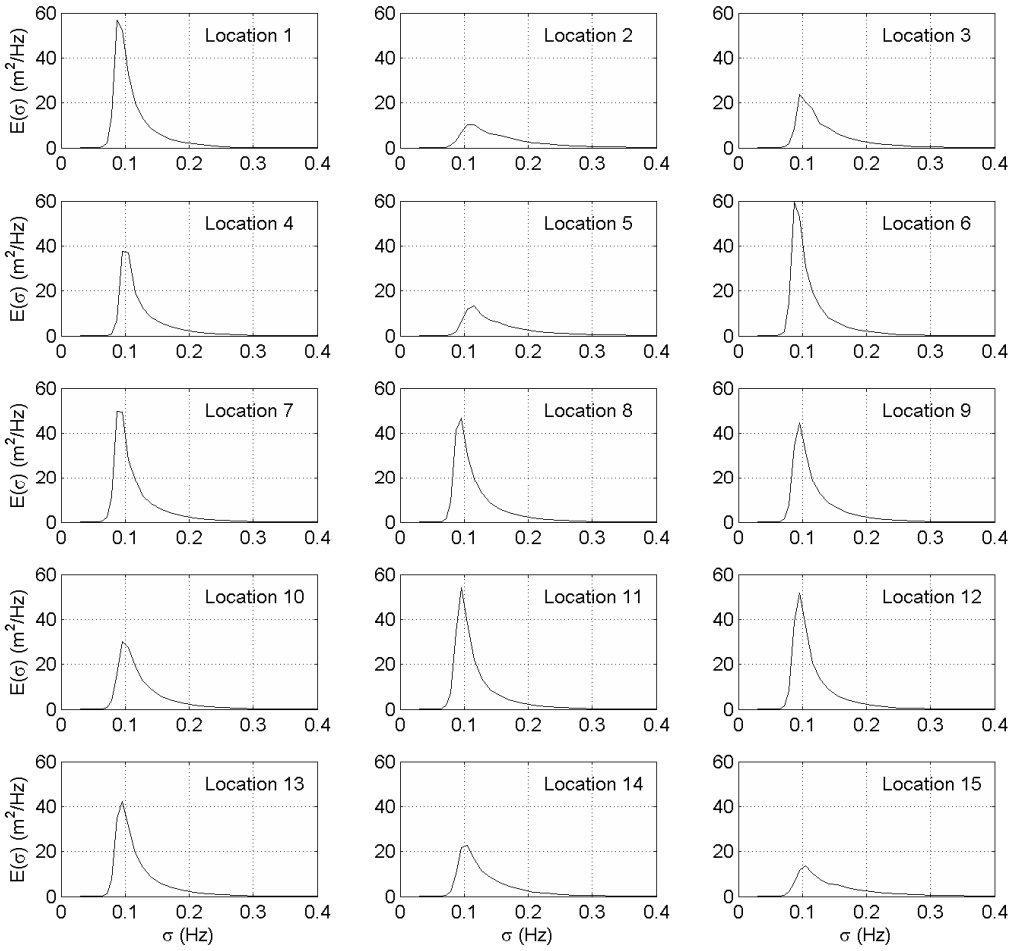

Figure E.2: One-dimensional wave spectra at fifteen locations in and near the Agulhas Current.

E.2 Cross sections

At location of the coastal jet and the anticyclonic ring (indicated in Figure E.3), cross sections of characteristic wave parameters and geographic distributions of the source- and propagation terms are presented in Figure E.5. These results are presented to easily notice the influence of the current on the waves and the wave-current interaction processes.

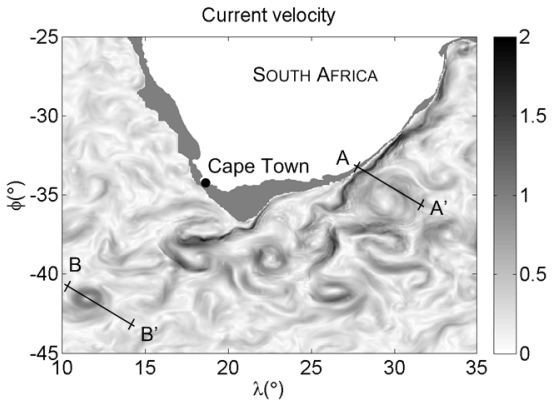

Figure E.3: As Figure E.2, with the indicated cross profile locations A-A' in the coastal jet and B-B' in the ring.

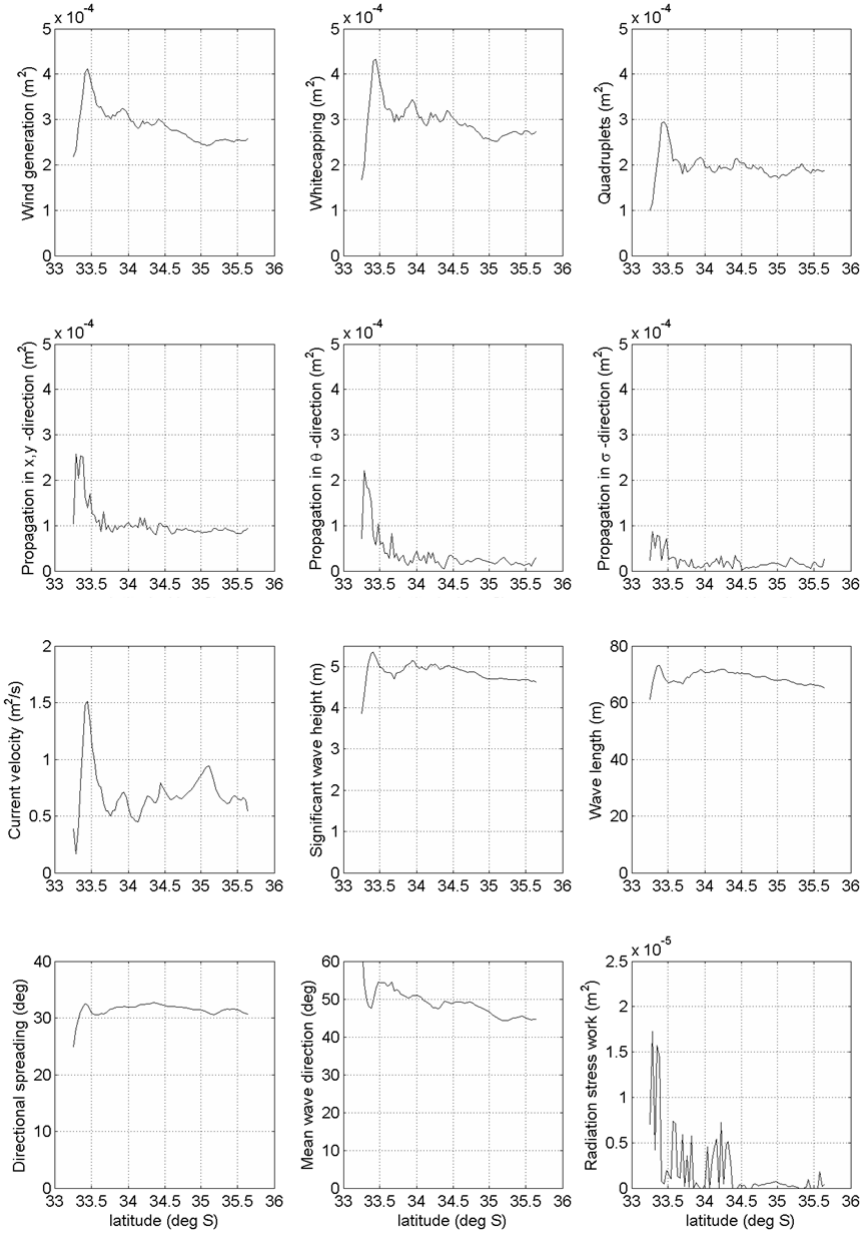

Figure E.4: Results SWAN at cross section A-A'.

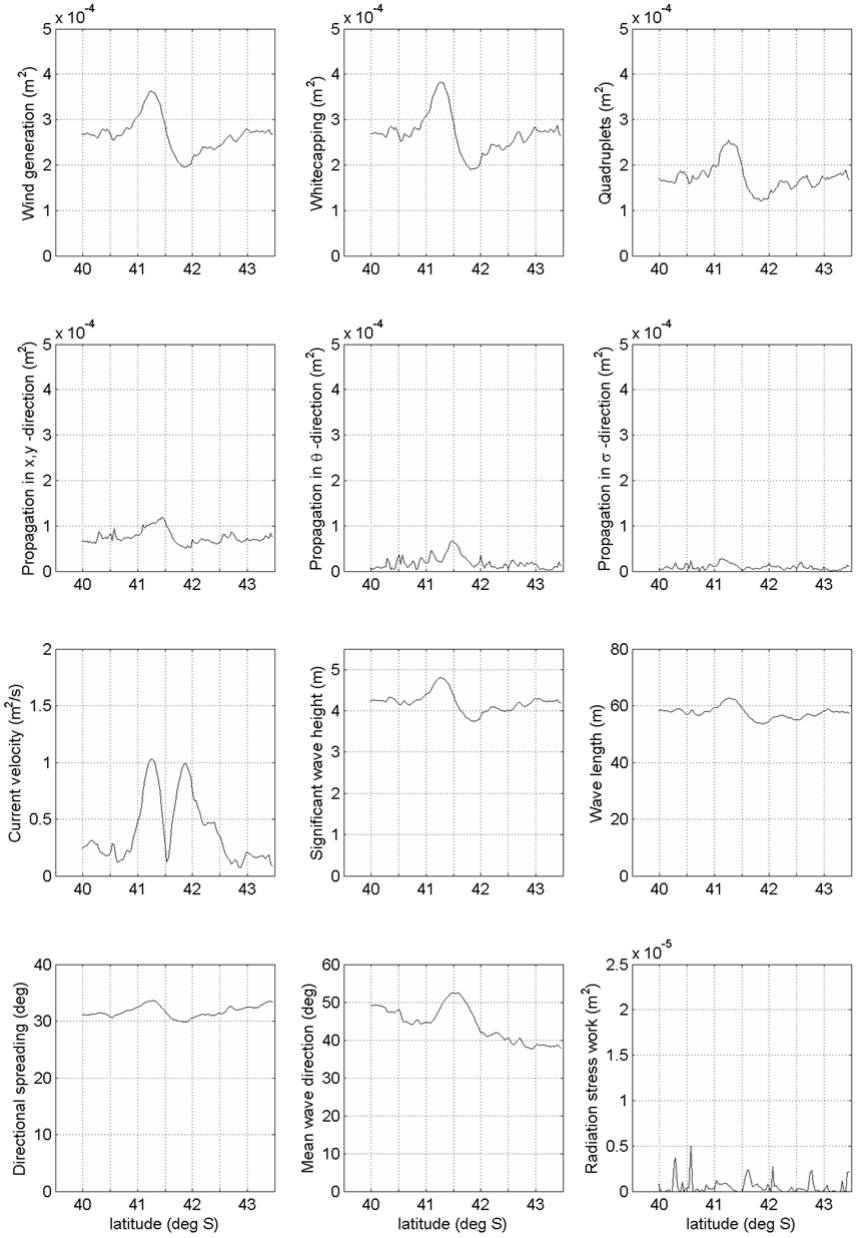

Figure E.5: Results SWAN at cross section B-B'.

References

Alves, J. H. G. M. and M. L. Banner, 2003, Performance of a saturation-based dissipation-rate source term in modelling the fetch-limited evolution of wind waves, *J. Phys. Oceanography*, **33**, 6, 1274-1298

Atlas of the Atlantic and Indian Ocean, 1977, Ministry of Defense of the USSR, pp. 204-207

Battjes, J. A. and J. P. F. M. Janssen, 1978, Energy loss and set-up due to breaking of random waves, *Proc. 16th Int. Conf. Coastal Engineering*, ASCE, 569–587

Benjamin, T.B., and J. E. Feir, 1967, The disintegration of wavetrains in deep water, Part 1, *J. Fluid Mech.*, **27**, 417-430

Booij, N., R. C. Ris and L. H. Holthuijsen, 1999, A third-generation wave model for coastal regions, Part I, Model description and validation, *J.Geoph. Res.*, **104**, C4, 7649-7666

Bottema, M., and G. Ph. Van Vledder, 2008, Effective fetch and non-linear four-wave interactions during wave growth in slanting fetch conditions, *Coastal Engineering*, **55**, 3, 261–275

Bretherton, F. P., and C. J. R. Garrett, 1969, Wavetrains in inhomogeneous moving media, *Proc. Roy. Soc.* A., **302**, 1471, 529-554

Draper, L., 1964, "Freak" ocean waves, *Oceanus*, **10**, 13–15

Dysthe, K. B., 1979, Note on a modification to the nonlinear Schrodinger equation for application to deep water waves, *Proceedings of the Royal Society of London. Series A, Mathematical and Physical Sciences*, **369**, 1736, 105-114

Dysthe, K. B., K. Trulsen, H. E. Krogstad, and H. Socquet-Juglard, 2003, Evolution of a narrow-band spectrum of random surface gravity waves, *J. Fluid Mech.*, **478**, 1–10

Dysthe, k. B., H. E. Krogstad,and P. Muller, 2008, Oceanic Rogue Waves, *Annu. Rev. Fluid Mech.*, **40**, 287–310

Forristall, G. Z., 2000, Wave crest distributions: observations and second order theory, *J. Phys. Ocean.*, **30**, 1931–1943

Gelci, R., Cazalé, H. and Vassal, J., 1957, Prévision de la houle. La méthode des densités spectroangulaires, Inform. Comité Central Océanogr. Etude Côtes 9, 416-435

Gerber, M., 1993, The interaction of deep-water gravity waves and an annular current: linear theory, *Journal of Fluid Mechanics*, **248**, 153-172

Gerber, M., 1996, Giant waves and the Agulhas Current, Deep-Sea Res. (submitted)

Gründlingh, M. L., 1994, Evidence of surface wave enhancement in the southwest Indian Ocean from satellite altimetry, *J. Geophys. Res.*, **99**, C4, 7917–7927

Gründlingh, M. L., and M. Rossouw, 1995, Wave attenuation in the Agulhas Current, *South African J. of Science*, **91**, 7, 357-361

Hasselmann, K., 1962, On the non-linear transfer in a gravity wave spectrum, part 1: General theory, *J. Fluid Mech.*, **12**, 481-500

Hasselmann, K., 1974, On the spectral dissipation of ocean waves due to white capping, *Boundary-Layer Meteorol.*, **6**, 1-2, 107-127

Hasselmann, S., K. Hasselmann, J. H. Allender and T. P. Barnett, 1985, Computations and parameterizations of the non-linear energy transfer in a gravity wave spectrum, part 2: Parameterizations of the non-linear transfer for application in wave models, *J. Phys. Oceanography*, **15**, 11, 1378-1391

Holthuijsen, L. H., and H. L. Tolman, 1991, Effects of the Gulf Stream on ocean waves, *J. Geophys. Res.,* **96**, C7, 12755–12771

Holthuijsen, L. H., 2007, Waves in oceanic and coastal waters, Cambridge University Press, 404 pp.

Holthuijsen, L. H., N. Booij, R. C. Ris, I. Haagsma, A. T. M. M. Kieftenburg, E. E. Kriezi, M. Zijlema, and A. J. van der Westhuysen, 2008, SWAN – User Manual, Technical report, Delft University of Technology, Environmental Fluid Mechanics Section, available from http://vlm089.citg.tudelft.nl/swan/index.htm (Version 40.72)

Hurdle, D. P., and G. Ph. Van Vledder, 2004, Improved spectral wave modelling of whitecapping dissipation in swell sea systems, *Proc. OMAE 2004*

Hwang, P. A., D. W. Wang, E. J. Walsh, W. B. Krabill, and R. N. Shift, 2000, Airborne measurements of the wavenumber spectra of ocean waves. Part 2. Directional distribution, *J. Phys. Oceanography*, **30**, 2768-2787

Janssen, P. A. E. M., 1991, Quasi-linear theory of wind-wave generation applied to wave forecasting, J. Phys. Oceanography, **21**, 1631-1642

Janssen, P. A. E. M., 2003, Non-linear four-wave interactions and freak waves, *J. Phys. Oceanography*, **33**, 4, 863-884

Kahma, K. K., and C. J. Calkoen, 1992, Reconciling discrepancies in the observed growth of wind-generated waves, *J. Phys. Oceanography*, **22**, 12, 1389–1405

Kenyon, K. E., 1971, Wave refraction in ocean currents, *Deep-Sea Res.*, **18**, 1023–1034

Kharif, C., and E. Pelinovsky, 2003, Physical mechanisms of the rogue wave phenomenon, *European Journal of Mechanics B/Fluids*, **22**, 603–634

Komen, G. J., S. Hasselmann and K. Hasselmann, 1984, On the existence of a fully developed wind-sea spectrum, J. Phys. Oceanography, 14, 1271-1285

Kuik, A. J., G. Ph. Van Vledder, and L. H. Holthuijsen, 1988, A method for the routine analysis of pitch-and-roll buoy wave data, J. Phys. Oceanography, 18, 7, 1020-1034

Lake, B. M., H. C. Yuen, H. Rungaldier,and W. E. Ferguson, 1977, Nonlinear deep-water waves: theory and experiment. Part 2: evolution of a continuous wave train, *J. Fluid Mech.*, **83**, 49–74

Lansen, A. J., 2006, Estimating freak wave occurrence probability in the Agulhas Current, M.Sc. Thesis, Technical report, Faculty of Civil Engineering and Geosciences, Delft University of Technology

Lavrenov, I. V., 1998, The wave energy concentration at the Agulhas Current off South Africa, *Natural Hazards*, **17**, 2, 117-127

Lavrenov, I. V., 2003, Wind-waves in oceans: dynamics and numerical simulations, Springer-Verlag Berlin Heidelberg New York

Liu, P. C., and K. R. MacHutchon, 2006, Are there different kinds of rogue waves, *25th International Conference on Offshore Mechanics and Arctic Engineering*, Hamburg, Germany

Longuet-Higgins, M. S., 1952, On the statistical distribution of the heights of sea waves, *J. Mar. Res.*, **11**, 245–265

Longuet-Higgins, M. S., 1957, The statistical analysis of a random, moving surface, *Philosophical Transactions of the Royal Society of London Series A*, **249**, 321–387

Longuet-Higgins, M. S., and R. W. Stewart, 1960, Changes in the form of short gravity waves on long waves and tidal currents, *Journal of Fluid Mechanics*, **8**, 4, 565-583

Longuet-Higgins, M. S., and R. W. Stewart, 1961, The changes in amplitude of short gravity waves on non-uniform currents, *Journal of Fluid Mechanics*, **10**, 4, 529-549

Longuet-Higgins, M. S., 1974, Breaking waves in deep and shallow water, *Proc. 10th Symp. Nav. Hydrodyn.*, 597–605

Lutjeharms, J. R. E., and R. C. van Ballegooyen, 1988, The retroflection of the Agulhas Current, *J. Phys. Oceanography*, **18**, 11, 1570–1583

Mallory, J. K., 1974, Abnormal waves on the south east coast of South Africa, *Int. Hydrog. Rev.*, **51**, 99-129

Marthinsen, T., and S. R. Winterstein, 1992, On the skewness of random surfaces. *Int Society of Offshore and Polar engineers*

Miles, J. W., 1957, On the generation of surface waves by shear flows, *J. Fluid Mech.*, **3**, 185-204

Mori, N., and P. A. E. M. Janssen, 2004, Dependence of freak wave occurrence on kurtosis. Rogue Waves 2004, Brest, France. Not published

Mori, N., M. Onorato, and P. A. E. M. Janssen, 2009, Directional dispersion effects on kurtosis for freak wave prediction. Rogue Waves 2008, Brest, France. Not published

Onorato, M., A. R. Osborne, and M. Serio, 2001, Extreme wave events in directional, random oceanic sea states, *Phys. Fluids*, **14**, 4, 25-28

Onorato, M., A. R. Osborne, and M. Serio, 2005, On deviations from Gaussian statistics for surface gravity waves, *Proceedings Rogue Waves, Hawaiian Winter Workshop*, 79-83

Onorato, M., A. R. Osborne, M. Serio, L. Caavaleri, C. Brandini, and C. T. Stansbert, 2006, Extreme waves, modulational instability and second order theory: wave flume experiments on irregular waves, *Eur. J. Mech. B/Fluids*, **25**, 586–601

Peregrine, D.H., 1976, Interaction of water waves and current. *Adv. Appl. Math.*, **16**, 9-117

Pierson, W. J., Jr., and L. Moskowitz, 1964, A proposed spectral form for fully developed wind seas based on the similarity theory of S. A. Kitaigorodskii, *J. Geophys. Res.*, **69**, 24, 5181–5190

Phillips, O. M., 1957, On the generation of waves by turbulent wind, *J. Fluid Mech.*, **2**, 417-445

Phillips, O. M., 1977, The dynamics of the upper ocean, Cambridge University Press, 336 pp.

Resio, D. T., and W. Perrie, 1991, A numerical study of nonlinear energy fluxes due to wave-wave interactions, part I, Methodology and basic results, *J. Fluid Mech.*, **223**, 609-629

Ris, R. C. and L. H. Holthuijsen, 1996, Spectral modelling of current induced wave-blocking, Proc. 25th Int. Conf. Coastal Engineering, ASCE, 1247–1254

Schumann, E. H., 1976, High waves in the Agulhas Current, *Mariners Weather Log.*, **20**, 1, 1-5

Seatre, R., and A. Jorge da Silva, 1984, The circulation of the Mozambique Channel, *Deep-Sea Res.*, **31**, 485–508

Smith, J. A., 2006, Wave-current interactions in finite depth, *J. Phys. Oceanography*, **36**, 7, 1403-1419

Snyder, R.L., Dobson, F.W., Elliott, J.A., and R.B. Long, 1981, Array measurement of atmospheric pressure fluctuations above surface gravity waves, *J. Fluid Mech.*, **102**, 1-59

Socquet-Juglard, H., K. Dysthe, K. Trulsen, H. Krogstad, and J. Liu, 2005, Probability distributions of surface gravity waves during spectral changes, *Journal of Fluid Mechanics,* **542**, 195-216

Tamura, H., T. Waseda, and Y. Miyazawa, Freakish sea state and swell-windsea coupling: Numerical study of the Suwa-Maru incident, *Geophys. Res. Let.*, **36**

Tracy, B. A., and D. T. Resio, 1982, Theory and calculation of the nonlinear energy transfer between sea waves in deep water, Technical report, WIS Report 11, US Army Corps of Engineers

Tulin, M. P., and T. Waseda, 1999, Laboratory observations of wave group evolution, including breaking effects, *J. Fluid Mech.*, **378**, 197–232

Vledder, G. Ph. van, 2001, Extension of the discrete interaction approximation for computing nonlinear quadruplet wave-wave interactions in operational wave prediction models, *Proc. 4th Int. Symp. on Ocean Wave Meas. and Analysis*

Vledder, G. Ph. van, and M. Bottema, 2003, Improved modelling of nonlinear four-wave interactions in shallow water, *Proc. 28th Int. Conf. Coastal Engineering*, ASCE, 459–471

Vledder, G. Ph. van, 2006, The WRT method for the computation of non-linear four-wave interactions in discrete spectral wave models, *Coastal Engineering*, **53**, 223–242

WAMDI Group, 1988, The WAM model – a third generation ocean wave prediction model, *J. Phys. Oceanography*, **18**, 1775-1810

Waseda, T., 2006, Impact of directionality on the extreme wave occurrence in a discrete random wave system, *Proc. 9th Int. Workshop Wave Hindcasting and Forecasting*, Victoria, Canada

Waseda, T., T. Kinoshita and H. Tamura, 2008, Evolution of a random directional wave and freak wave occurrence, *J. Phys. Oceanography,* Preliminary issue

Webb, D. J., 1978, Non-linear transfers between sea waves, *Deep-Sea research*, **25**, 3, 279-298

Westhuysen, A. van der, M. Zijlema, and J.A. Battjes, 2005, Improvement of the numerics and deep-water physics in an academic version of SWAN, *Proc. 29th Int. Conf. Coastal Engineering, ASCE*, 855-867

Westhuysen, A. van der, M. Zijlema and J.A. Battjes, 2007, Nonlinear saturation-based white capping dissipation in SWAN for deep and shallow water, *Coastal Engineering*, **54**, 2, 151-170

White, B. S., and B. Fornberg, 1998, On the chance of freak waves at sea, *J. Fluid Mech.*, **355**, 113–138

Whitman, G. B., 1962, Mass, momentum and energy flux in water waves, *Journal of Fluid Mechanics*, **12**, 1, 135-147

Yan, L., 1987, An improved wind input source term for third-generation ocean wave modelling, Scientific Report WR-No 87-8, De Bilt, KNMI

Young, I.R., and G. Ph. van Vledder, 1993, A review of the central role of nonlinear interactions in wind-wave evolution, *Phil. trans. R. Soc. London.* A., **342**, 505-524

Zakharov, V. E., 1968, Stability of periodic waves of finite amplitude on the surface of a deep fluid, *Journal of Applied Mechanics and Technical Physics*, **9**, 190–194

Zakharov, V. E., A. I. Dyachenko, and A. O. Prokofiev, 2006, Freak waves as nonlinear stages of Stokes wave modulation instability, *Eur. J. Mech. B/Fluids*, **25**, 667–692

Zijlema, M., 2005, Parallelization of a nearshore wind wave model for distributed memory architectures. *In: G. Winter, A. Ecer, J. Periaux, N. Satofuka and P. Fox, Editors, Parallel Computational Fluid Dynamics - Multidisciplinary Applications*, Elsevier, 207-214

List of figures

List of tables

Nomenclature

Roman letters

a	Wave amplitude
A	Normalization coefficient
c	Phase velocity
C_{ds}	Whitecapping coefficient
c_g	Group velocity
$c_{g;\lambda}$	Propagation velocity of wave energy in λ-space
$c_{g;\varphi}$	Propagation velocity of wave energy in φ-space
c_σ	Propagation velocity of wave energy in frequency space
c_θ	Propagation velocity of wave energy in spectral space
dl, dk	Perturbation wavenumber
E	Energy density
g	Gravity constant
k	Wavenumber
k_0	Envelope wavenumber
k_p	Peak wavenumber of the wavenumber spectrum
H_s	Significant wave height
$H_{\max}$	Maximum wave height
K	Spectral bandwidth of the wavenumber spectrum
l	Unit vector
L_m	Mean wavelength
m	m is a coordinate perpendicular to the wave crest
m_n	n-th order moment of the energy density spectrum
n	n is a coordinate normal to the wave crest
N	Action density
Q_b	Fraction of breaking waves Battjes and Janssen (1978)
Q_p	Goda parameter of peakedness parameter Goda (1970)
S_{nl4}	Source term of quadruplet wave-wave interactions
S_{tot}	Sum of all source terms
S_{wcap}	Source term of whitecapping dissipation
S_{wind}	Source term of generation by wind

t	Time
T_{m01}	Relative mean wave period
T_p	Peak period
U	Current velocity
u_*	Friction velocity
U_{10}	Wind speed at 10 m above sea surface
x	x-coordinate
y	y-coordinate

Greek letters

α	Random phase
α_{BJ}	Constant in depth-induced wave breaking formulation
β	Coefficient of the wind-induced wave growth
ε	Steepness
ε_{eff}	Effective steepness
ε_{PM}	Steepness for the Pierson and Moskowitz (1964) spectrum
Φ	Wave-induced radiation stress
γ	Peak enhancement factor of the JONSWAP spectrum
λ,φ	Spherical coordinates, longitude and latitude, respectively
ρ_a	Density of air
ρ_w	Density of water
Γ, Γ_{KJ}	Steepness dependent coefficients in whitecapping formulations
Δx	Increments in geographical x - space
Δy	Increments in geographical y - space
$\Delta\sigma$	Increments in relative frequency space
$\Delta\theta$	Increments in directional space
η	Surface elevation
κ	Nonlinearity parameter
κ_{40}	Kurtosis of the surface elevation
θ	Direction normal to the wave crest
σ	Relative frequency
σ_p	Relative peak frequency
σ_θ	Directional spreading
σ_ω	Spectral width
ω_0	Absolute frequency
ψ	Phase for the complex field

Other

∂	Partial differentiation operator

Acronyms

BFI	Benjamin Feir Instability parameter
DIA	Discrete Interaction Approximation (quadruplet interaction model)
JONSWAP	Joint North Sea Wave Project
NRL	Naval Research Laboratory
NLOM	NRL Layered Ocean Model
NOGAPS	Navy operational Global Atmospheric Prediction System
SWAN	Simulating Waves Nearshore
WRT	Webb-Resio-Tracy (exact quadruplet interaction model)
XNL	Exact quadruplet interaction method in SWAN